



The capture probability of Dawn into ground-track resonances with Vesta

Wail Boumchita¹ · Jinglang Feng¹

Received: 19 May 2023 / Revised: 7 November 2023 / Accepted: 3 December 2023 /

Published online: 19 December 2023

© The Author(s) 2023

Abstract

The Dawn spacecraft approached the asteroid Vesta and descended from a high-altitude mission orbit to a low-altitude mission orbit using low-thrust propulsion. During this descent, the spacecraft crossed the 2:3 and 1:1 ground-track resonances with Vesta, which posed a risk of capture that might strongly perturb the spacecraft's orbit. This study analyzes the effects of these resonances on the spacecraft's orbital elements and estimates the probability of capture into it through Monte Carlo simulations. Specifically, a comprehensive investigation is performed to assess the effects of 1:1 and 2:3 ground-track resonances on the semimajor axis, eccentricity, and inclination. The dynamical model includes the gravitational field of Vesta using a spherical harmonics approximation up to the fourth degree and order and the low-thrust acceleration that is assumed to be opposite to the spacecraft's velocity vector direction. It is observed that the eccentricity evolution is mostly influenced by the 2:3 ground-track resonance which results in a large variation when the spacecraft crosses that ground-track resonance, while the semimajor axis and inclination are mostly influenced by the 1:1 ground-track resonance. Then, the probability of capture into 1:1 ground-track resonance is found to have a negative correlation with the spacecraft's thrust magnitude and the probability of capture into 2:3 ground-track resonance is found to arise as the spacecraft's mass increases. It is found that for circular orbits below a certain inclination value the spacecraft's trajectory is subject to the "automatic entry into libration" phenomenon, due to the singularity in the Hamiltonian function. This research contributes to the design of successful transfer strategies when crossing resonance for future missions.

Keywords Vesta · Irregular gravitational perturbations · Low-thrust propulsion · Resonance capture · Automatic entry into libration

✉ Wail Boumchita
wail.boumchita@strath.ac.uk

✉ Jinglang Feng
jinglang.feng@strath.ac.uk

¹ Department of Mechanical and Aerospace Engineering, University of Strathclyde, 75 Montrose Street, Glasgow G1 1XJ, Scotland, UK

1 Introduction

Resonance is a pervasive phenomenon in dynamical systems, arising when a system is excited at its natural frequency, thereby causing pronounced oscillations. This concept manifests across diverse disciplines, including plasma physics (Artemyev et al. 2018), celestial mechanics (Garfinkel 1982), and astrodynamics (Tricarico and Sykes 2010). Within the realms of celestial mechanics and astrodynamics, various forms of orbital resonances are evident. These range from mean motion resonances, where the orbital periods of two celestial bodies are in simple integer ratios (Murray and Dermott 2000), to more complex forms like secular (Celletti et al. 2020), secondary (Lemaître et al. 2009), spin-orbit (Goldreich and Peale 1966), and ground-track resonances (GTRs) (Tricarico and Sykes 2010). Notably, for GTRs to manifest, the period of a spacecraft's revolution must be commensurable with the rotation period of the central body, as exemplified in 1:1 GTRs with Earth's geostationary satellites (Celletti and Gales 2014). Previous studies have delved into the impact of irregular gravitational fields on resonant satellite orbits. Scheeres (1994) focused on satellites orbiting irregularly shaped asteroids, particularly investigating periodic orbits around the ellipsoids mimicking asteroids Vesta and Eros. Subsequent extensions of this work explored the asteroid Toutatis (Scheeres et al. 1998) and the moons Europa (Scheeres et al. 2001; Paskowitz and Scheeres 2006; Russell 2006) and Enceladus (Lara and Russell 2010; Russell and Lara 2009).

In 2011, the Dawn spacecraft successfully approached the asteroid Vesta (Russell et al. 2007), and it was one of the first missions to use low-thrust propulsion during both the cruise phase and the approach phase to an asteroid. This mission demonstrated the possibility of relying on low-thrust propulsion for the majority of the mission duration (Rayman 2020; Wallace et al. 2019; Nishiyama et al. 2016). The use of low-thrust propulsion allows for more efficient use of fuel and longer mission duration but also poses challenges in terms of trajectory design (Morante et al. 2021). One major challenge when using low-thrust propulsion during the approach to an asteroid is the probability of being captured by 1:1 GTR (Tricarico and Sykes 2010), caused by the chaotic layer surrounding the resonance region (Celletti and Gales 2014). The spacecraft at each revolution encounters the same gravitational configuration, the effect of which may accumulate and significantly change the orbit eccentricity and inclination (Scheeres 2012). The capture of a spacecraft into a GTR has the potential to significantly impact the success of a mission by preventing it from reaching lower altitudes and the achievement of scientific objectives.

For this reason, it is important to investigate the probability of capture into the GTR of a spacecraft around an asteroid. This necessitates a comprehensive understanding of the dynamics of both the spacecraft and the asteroid. The outcomes of these studies can be utilized to ensure the robustness of the mission. Tricarico and Sykes (2010) investigated the possibility of the Dawn spacecraft being captured into the 1:1 GTR around Vesta, located within the orbital radius range of 500 and 600 km. The authors simulated the descent starting from 1000 km and considered 12 different initial conditions, which were shifted by an angle of 30° of true anomaly. Out of the 12 simulations conducted, capture occurred only once, yielding an estimated capture probability of $1/12$ based on this limited sample size. Delsate (Delsate 2012) extended this analysis using a larger set of initial conditions and varying thrust magnitudes, thereby achieving a similar capture probability of 8.26%, albeit with enhanced reliability due to the increased number of simulations. It was found that the probability of capture into GTR is dependent on various factors such as the initial state of the spacecraft, the thrust magnitude, and the characteristics of the central body. In this research, we improve the understanding of the 1:1 and 2:3 GTRs by investigating their effect on the semimajor

Table 1 Vesta's physical parameters (Tricarico and Sykes 2010)

Gravitational constant	μ	$17.5 \text{ km}^3/\text{s}^2$
Reference radius	R_e	300 km
Angular velocity	$\dot{\theta}$	$3.2671 \times 10^{-4} \text{ rad/s}$

axis, eccentricity, and inclination and by considering a larger interval of thrust magnitude and spacecraft's mass values. Additionally, this research offers important insights into the sensitivity of the probability of capture into GTRs on the initial orbit geometry. The methodology used in this work can be readily used for a wide variety of space exploration missions.

The structure of this paper is as follows: Sect. 2 presents the equations of motion and defines the Hamiltonian dynamical model. It characterizes the phase-space and provides important insights into the phenomenon of the GTR. Section 3 focuses on the analysis of the effects of the 1:1 and 2:3 GTRs on Dawn's descent trajectory, specifically the effect of the accumulation of gravitational perturbation on the evolution of the semimajor axis, eccentricity, and inclination. Section 4 conducts a sensitivity analysis of the probability of capture on different values of thrust magnitude, spacecraft mass, and initial inclination. Finally, a summary of the paper and the conclusions are presented.

2 Dynamical modeling

In this section, the dynamical environment surrounding Vesta is investigated to identify perturbations that need to be considered for the modeling of the dynamics. Subsequently, the physical and gravitational characteristics of Vesta and the equations of motion for the spacecraft are presented. The Hamiltonian function of the system is then defined and the dynamics of the Dawn mission phase-space are investigated.

2.1 Main perturbations

In 2011, the Dawn spacecraft successfully arrived at the asteroid Vesta. During the approach phase, the spacecraft descended from a high-altitude mission orbit (HAMO) to a low-altitude mission orbit (LAMO) utilizing low-thrust propulsion. The orbital radii of the HAMO and LAMO are 1000 and 460 km, respectively (Tricarico and Sykes 2010). However, the use of low-thrust propulsion during the descent phase posed a risk of capturing the spacecraft into GTRs around Vesta. The physical parameters of Vesta are listed in Table 1, and it is assumed to rotate uniformly around a constant direction in the inertial frame, coinciding with the axis of symmetry of the gravitational field. The unnormalized Stokes coefficients of Vesta are given in Feng et al. (2017).

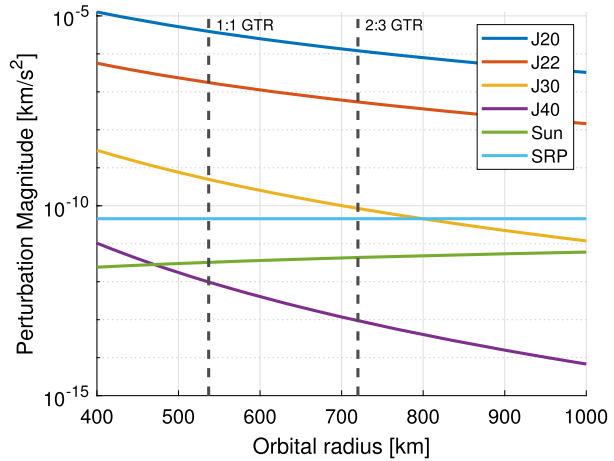
The spacecraft is subject to the following perturbations (Montenbruck et al. 2002):

- Vesta's irregular gravitational perturbations

$$a_{nm} = (n+1) \frac{\mu}{r^2} \frac{R_e^n}{r^n} J_{nm};$$

$$\text{where } J_{nm} = \sqrt{C_{nm}^2 + S_{nm}^2}.$$

Fig. 1 Order of magnitude of the various perturbations to which the Dawn spacecraft is subject at different orbital radii. The location of the 1:1 and 2:3 GTRs is highlighted for reference



- Sun's gravitational perturbation

$$a_{\text{Sun}} = \frac{2\mu_{\odot}}{d_{\odot}^3} r;$$

- solar radiation pressure perturbation

$$a_{\text{SRP}} = C_r \frac{A}{m} P_{\odot}$$

where r represents the distance from the spacecraft to Vesta, C_{nm} and S_{nm} are the unnormalized Stokes coefficients, n and m are the degree and order of the spherical harmonic expansion element considered, μ_{\odot} represents the gravitational constant of the Sun, d_{\odot} is the distance of the spacecraft from the Sun, $C_r = 0.25$ is the reflectivity coefficient of the spacecraft, $A/m = 0.04 \text{ m}^2/\text{kg}$ is the area-to-mass ratio of the spacecraft, and P_{\odot} is the solar radiation pressure at a distance d_{\odot} from the Sun. The magnitudes of the main perturbations at different orbital radii are illustrated in Fig. 1.

A thorough analysis of the figure reveals that at the orbital radius corresponding to the 1:1 GTR, i.e., 537 km, Vesta's second degree gravitational perturbations are a few orders of magnitude stronger than the perturbations from the Sun's gravitational attraction, and the solar radiation pressure. This highlights the importance of accurately accounting for Vesta's gravitational influence in the dynamical modeling of the spacecraft's trajectory. Furthermore, it is worth noting that the relative magnitudes of these perturbations can vary significantly depending on the orbital radius of the spacecraft. Given the dominant effect of Vesta's irregular gravitational perturbations at the 2:3 GTR and 1:1 GTR and the potential impact on the spacecraft's trajectory, in this paper, only these perturbations are considered in the dynamical modeling; solar gravitation and solar radiation pressure are ignored in the following analysis.

2.2 Equations of motion

The literature provides several methods for representing the gravitational field of a celestial body.

- The polyhedron approximation method (Werner 2017) involves approximating the volume of an asteroid as a polyhedron and determining the gravitational field by summing the

contributions of each volumetric element. This method offers a simplified representation of the asteroid's gravitational field, but its accuracy may be limited by the precision of the polyhedron approximation. The accuracy of this method can be improved by increasing the number of individual terms used, but this comes at the cost of increased computational cost.

- The point mass approximation method, as described in Barthelmes and Dietrich (1991), generates a gravitational field approximation by treating the asteroid as a set of discrete point masses. While this method is less accurate compared to the polyhedron method, it is computationally more efficient. The accuracy of this method can be improved by increasing the number of point masses used, but this comes at the cost of increased computational cost.
- The spherical harmonics approximation is a commonly used method for characterizing the gravitational field of celestial bodies (Montenbruck et al. 2002; Kaula 1966). This method is based on the expansion of the gravitational potential in terms of spherical harmonics, which are a set of orthogonal functions defined on the surface of a sphere. This approach maintains a balance between accuracy and computational cost and has been extensively employed in prior studies (Tricarico and Sykes 2010; Delsate 2012; Feng et al. 2017; Whiffen 2004). In these works, the spherical harmonics approximation was applied to multiple asteroids, including Vesta, 1996 HW1, Betulia and for a generic asteroid shape. In this paper, we apply this methodology to approximate Vesta's irregular gravitational field.

The gravitational potential of a central body is defined as a function of spherical harmonics, where the shape and density variations of the asteroid are represented by the Stokes coefficients. The gravitational potential V , in spherical harmonics expansion of degree n and order m , is given in spherical coordinates (r, δ, ϕ) as

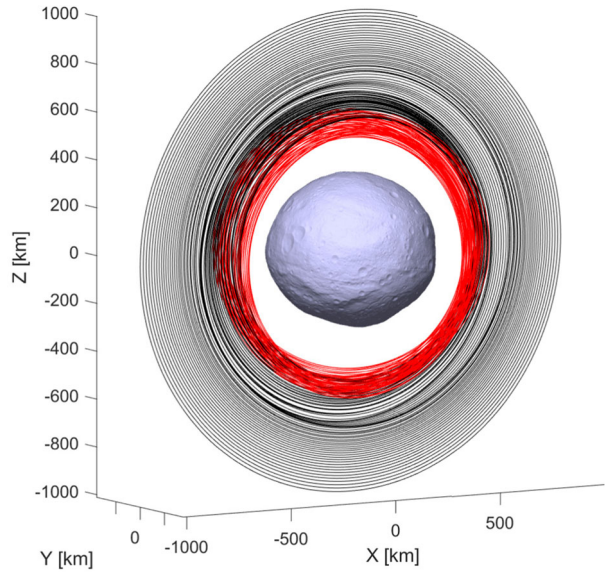
$$V = \frac{\mu}{r} + \sum_{n=2}^{\infty} \sum_{m=0}^n \frac{\mu}{r} \left(\frac{R_e}{r} \right)^n P_{nm}(\sin \phi) (C_{nm} \cos m\delta + S_{nm} \sin m\delta), \quad (1)$$

where ϕ and δ are the colatitude and the longitude, respectively. Previous studies have shown that the dynamics around Vesta are primarily influenced by the spherical harmonics expansion up to the fourth degree and order (Tricarico and Sykes 2010). This is also the truncation order adopted in our current study. Our simulations focus on the perturbed two-body problem (Whiffen 2004), where the spacecraft is subject to perturbations from Vesta's irregular gravitational field and a constant low-thrust acceleration in the direction opposite of the spacecraft's velocity. In this way, the semimajor axis decreases in the most efficient way (Huang et al. 2020). The equations of motion in cartesian coordinates and in the asteroid's centered inertial frame are

$$\begin{cases} \ddot{\mathbf{x}} = \nabla V - \frac{T}{m(t)} \hat{\mathbf{v}} \\ \dot{m} = -\frac{T}{I_{sp} g_0} \end{cases}, \quad (2)$$

where $\mathbf{x} = [x, y, z]$ is the position vector in cartesian coordinates, $\ddot{\mathbf{x}} = [a_x, a_y, a_z]$ is the acceleration vector, V represents the potential in spherical harmonics in Eq. 1, T is the thrust magnitude, m is the spacecraft's mass, and $\hat{\mathbf{v}}$ is the spacecraft's velocity unit vector. Finally, the second equation describes the rate of change of the spacecraft's mass over time as a function of I_{sp} and g_0 which represent the specific impulse and Earth's gravitational constant, respectively. The equations of motion are propagated using the MATLAB built-in function `ode113` which is a variable-step, variable-order Adams–Bashforth–Moulton solver

Fig. 2 Sample of a trajectory captured into GTR with Vesta. The black line represents the first part of the descent; the red line represents the trajectory after the capture has occurred



of orders 1–13 (Shampine and Gordon 1975), with a relative and absolute tolerance set at 10^{-12} . Figure 2 shows a sample of a trajectory captured into GTR in the asteroid's centered inertial frame.

2.3 Hamiltonian model

The Hamiltonian formalism is an effective method for analyzing resonance dynamics. The gravitational field, as defined in Eq. 1, can be represented as a function of orbital elements, as Kaula (1966)

$$V = \frac{\mu}{r} + \sum_{n=2}^{\infty} \sum_{m=0}^n \sum_{p=0}^n \sum_{q=-\infty}^{\infty} \frac{\mu R_e^n}{a^{n+1}} F_{nmp}(i) G_{npq}(e) S_{nmpq}(\omega, M, \Omega, \theta), \quad (3)$$

where $F_{nmp}(i)$ and $G_{npq}(e)$ are functions of the inclination i and eccentricity e , respectively, ω represents the argument of periapsis, M is the mean anomaly, Ω denotes the longitude of the ascending node, θ represents the sidereal time, n, m, p, q are integers, and

$$S_{nmpq} = \begin{cases} C_{nm} \cos \Psi_{nmpq} + S_{nm} \sin \Psi_{nmpq}, & \text{if } n - m \text{ is even} \\ -S_{nm} \cos \Psi_{nmpq} + C_{nm} \sin \Psi_{nmpq}, & \text{if } n - m \text{ is odd} \end{cases},$$

where Ψ_{nmpq} is Kaula's phase angle that is defined as

$$\Psi_{nmpq} = (n - 2p)\omega + (n - 2p + q)M + m(\Omega - \theta), \quad (4)$$

GTRs occur when the rate of change of Kaula's phase angle $\dot{\Psi}_{nmpq}$ is close to zero, i.e., when the phase angle of the system remains relatively constant over time.

By defining the quantity $L = \sqrt{\mu a}$ as the conjugate momentum to $\lambda = M + \Omega + \omega$, the Hamiltonian that describes the motion of the spacecraft around an asteroid with an irregular

Table 2 Spherical harmonics terms related to the 1:1 GTR up to 2nd degree and order ($e = 0$) (Kaula 1966)

n	m	p	q	Ψ_{nmpq}	F_{nmp}	G_{npq}
2	0	1	0	0	$3/4 \sin^2 i - 1/2$	1
2	2	0	0	$2\lambda - 2\theta$	$3(1 + \cos i)^2/4$	1

gravitational field can be defined as

$$\mathcal{H} = -\frac{\mu^2}{2L^2} + \sum_{n=2}^{\infty} \sum_{m=0}^n \sum_{p=0}^n \sum_{q=-\infty}^{\infty} R_e^n \frac{\mu^{n+2}}{L^{2n+2}} F_{nmp}(i) G_{npq}(e) S_{nmpq}(\omega, M, \Omega, \theta) + \dot{\theta} \Lambda, \quad (5)$$

where Λ is the conjugated momentum to the sidereal time θ and the term $\dot{\theta} \Lambda$ accounts for the asteroid's rotation. The dynamics of the system close to the 1:1 GTR are primarily affected by the gravitational term up to the second degree and order (Scheeres 1999). In light of this, the Hamiltonian used in the analysis is limited to the second degree and order. The harmonic contributions incorporated in the potential V are selected based on the resonance under consideration. In the case of the 1:1 GTR, the harmonics that contribute to this resonance are listed in Table 2.

For a polar circular orbit, the Hamiltonian is

$$\begin{aligned} \mathcal{H}_{1:1} = & -\frac{\mu^2}{2L^2} + \frac{1}{4} R_e^2 \frac{\mu^4}{L^6} C_{20} \\ & + \frac{3}{4} R_e^2 \frac{\mu^4}{L^6} \sqrt{C_{22}^2 + S_{22}^2} \cos \left[\Psi_{2200} + \arctan \left(-\frac{S_{22}}{C_{22}} \right) \right] + \dot{\theta} \Lambda, \end{aligned} \quad (6)$$

where the first argument of the cosine is

$$\Psi_{2200} = 2(M + \Omega + \omega) - 2\theta = 2(\lambda - \theta). \quad (7)$$

The resonance angle σ in the case of 1:1 GTR is

$$\sigma = \lambda - \theta. \quad (8)$$

However, in order to preserve a set of canonical variables, it is necessary to perform a canonical transformation. These transformations are important in Hamiltonian mechanics as they allow for the definition of new variables that can simplify the analysis of the Hamiltonian function. In this particular case, the canonical transformation proposed by Valk et al. (2009) is adopted. The new set of variables is

$$\sigma, \quad L' = L, \quad \theta' = \theta, \quad \Lambda' = \Lambda + L.$$

As a result of this transformation, the new Hamiltonian is

$$\begin{aligned} \tilde{\mathcal{H}}_{1:1} = & -\frac{\mu^2}{2L^2} - \frac{1}{4} R_e^2 \frac{\mu^4}{L^6} C_{20} \\ & - \frac{3}{4} R_e^2 \frac{\mu^4}{L^6} \sqrt{C_{22}^2 + S_{22}^2} \cos \left[2\sigma + \arctan \left(-\frac{S_{22}}{C_{22}} \right) \right] - \dot{\theta} L, \end{aligned} \quad (9)$$

in which the prime signs are dropped for simplicity and the constant $\dot{\theta} \Lambda'$ term is not included since the expression is no more explicitly dependent on θ . For Vesta, $S_{22} = 0$ (Tricarico and Sykes 2010), so the Hamiltonian is simplified to

$$\tilde{\mathcal{H}}_{1:1} = -\frac{\mu^2}{2L^2} - \frac{1}{4} R_e^2 \frac{\mu^4}{L^6} C_{20} - \frac{3}{4} R_e^2 \frac{\mu^4}{L^6} C_{22} \cos 2\sigma - \dot{\theta} L. \quad (10)$$

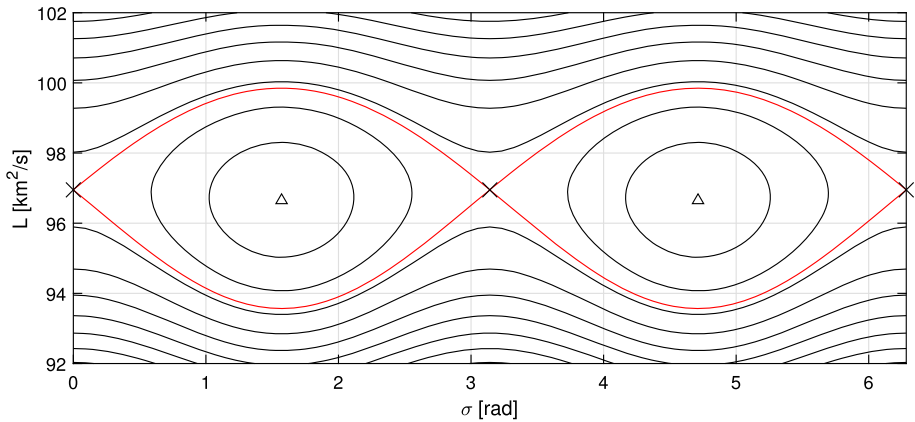


Fig. 3 Phase-space configuration of the 1:1 GTR around Vesta. The black curves are the different energy levels, while the red lines are the separatrices that enclose the two GTR regions. The stable and unstable equilibrium points are indicated with a triangle and a cross, respectively

Generally, when considering a gravitational field up to the second degree and order, four equilibrium points can be identified. Two of them are always unstable, while the other two may be either stable or unstable, depending on the physical characteristics of the asteroid, such as its rotational rate, second degree gravity coefficients, and mass (Hu and Scheeres 2004). By analyzing the Hamiltonian $\tilde{\mathcal{H}}_{1:1}$ defined in Eq. 10, it is possible to find two stable equilibria σ_{st} and two unstable equilibria σ_{un} , as solutions of

$$\frac{\partial \tilde{\mathcal{H}}_{1:1}}{\partial L} = \frac{\partial \tilde{\mathcal{H}}_{1:1}}{\partial \sigma} = 0, \quad (11)$$

which are

$$\sigma_{un} = 0, \quad \sigma_{un} = \pi, \quad \sigma_{st} = \pi/2, \quad \sigma_{st} = 3/2\pi. \quad (12)$$

These equilibrium points are the locations in the phase-space where the spacecraft's motion is stationary in the body-fixed frame (Boccaletti and Pucacco 2001). Figure 3 shows the phase-space of the 1:1 GTR from Eq. 10, where the stable and unstable equilibrium points are indicated with a triangle and a cross, respectively.

The region of interest, also known as the resonance region, is confined between the two red curves, known as separatrices. The regions above and below the resonance region are referred to as the upper and lower circulation regions, respectively. In the phase-space, the conjugate momentum L is plotted along the y-axis and is closely related to the semimajor axis of the orbit. As the spacecraft is descending to a lower altitude orbit, it crosses the resonance region from a higher altitude orbit and exits the resonance from a lower altitude, finally reaching the target orbit. So, in phase-space, the trajectory starts in the upper circulation region, crosses the upper separatrix, then crosses the lower separatrix, and finally reaches within the lower circulation region. When the spacecraft is captured into GTR, its trajectory in the phase-space is confined to the resonance region, and it oscillates around the stable equilibrium point σ_{st} as shown in the upper plots of Fig. 4. On the other hand, if no GTR capture occurs, the spacecraft's trajectory in the phase-space escapes the resonance region and reaches the lower circulation region, as shown in the lower plots of Fig. 4.

From the left plots of Fig. 4, it can be difficult to determine the precise moment of separatrix crossing. To alleviate this issue, the following steps are implemented:

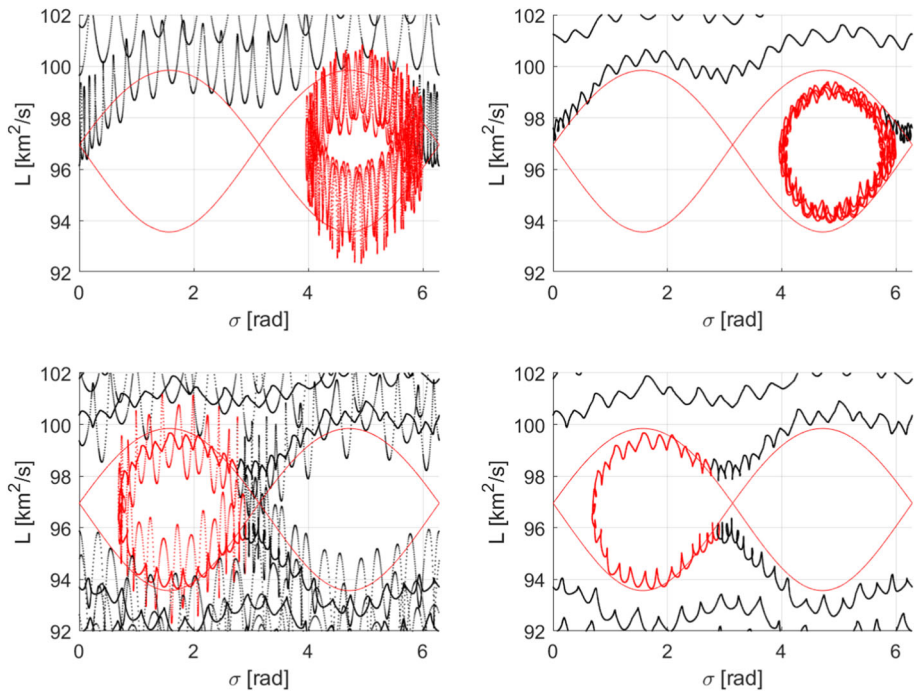


Fig. 4 Trajectories of the spacecraft's descent in the case of captured (upper plots) and escape (lower plots) from the 1:1 GTR in phase-space. In the plots on the left, the true trajectories are plotted, while on the right the same trajectories after averaging are plotted. The trajectory lines are red when inside the resonance region

- The trajectory in the phase-space is averaged to eliminate high-frequency oscillations and improve the clarity of the trajectory's evolution making it easier to identify the point of entry into resonance. Different from the conventional orbital average over one orbital revolution, we compute the moving average using MATLAB's built-in function, `movmean`. Commonly known as a rolling or running average, this technique produces a series of averaged values from different subsets of the original data set. While primarily employed in time series analysis, the moving average serves to smooth out short-term fluctuations, thereby highlighting underlying long-term trends or cyclical patterns. Mathematically, the moving average, denoted as \bar{L} , for a time series $L = [L_1, L_2, L_3, \dots, L_n]$ is given as follows:

$$\bar{L}_i = \frac{1}{z} \sum_{j=0}^{z-1} L_{i-j}, \quad (13)$$

where z is the length of the moving average window.

- The point of entry into resonance with Vesta is defined as the point at which the averaged trajectory crosses the upper separatrix line. This step allows for a well-defined criterion to identify the point of entry into resonance.

The right plots of Fig. 4 show the result of these steps on the trajectory, where the captured part of the descent can be clearly recognized. To identify the moment of separatrix crossing, the Hamiltonian function is evaluated at each instant and compared to the value of the Hamiltonian at the separatrix $\mathcal{H}_{1:1}^{\text{sep}}$. When the two values coincide, the spacecraft enters into

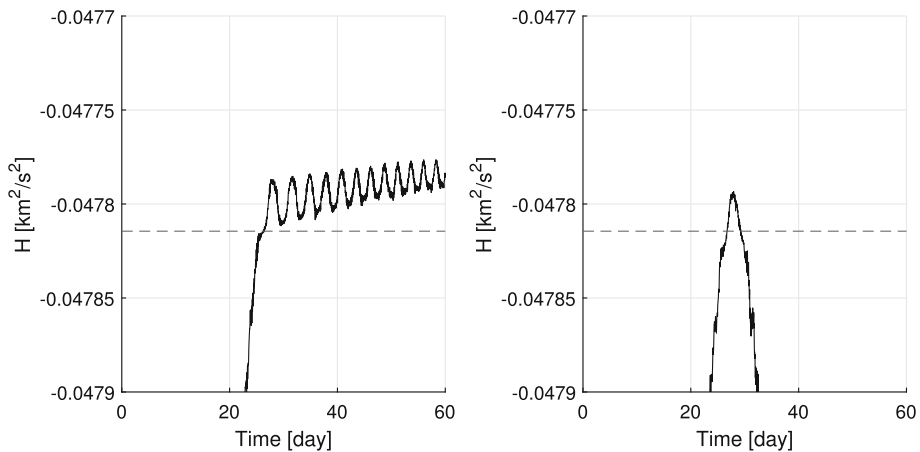


Fig. 5 Hamiltonian evolution during the descent of the spacecraft from a circular polar orbit at 1000 km. The left plot represents the capture case, while the right plot represents the escape case. The dashed line represents the value of the Hamiltonian at the separatrix

Table 3 Dawn's nominal initial conditions at HAMO (Tricarico and Sykes 2010)

Mass	m	1000 kg
Thrust magnitude	T	20 mN
Specific impulse	I_{sp}	3000 s
Semimajor axis	a_0	1000 km
Eccentricity	e_0	0
Inclination	i_0	90°
Longitude of the ascending node	Ω_0	0°
Argument of periapsis	ω_0	0°

the resonance region. If the value of the Hamiltonian function coincides for a second time with the value $\mathcal{H}_{1:1}^{sep}$, the trajectory escapes from the resonance and enters into the lower circulation region. As shown in Fig. 5, the evolution of the system's Hamiltonian is compared with the Hamiltonian value at the separatrix, indicated by the horizontal dashed line. On the left panel, the Hamiltonian crosses the separatrix value only once as the spacecraft is captured into a 1:1 GTR. On the contrary, in the right panel, the Hamiltonian crosses the separatrix value a second time as the spacecraft escapes from the GTR.

3 GTRs capture

Throughout the paper, the Dawn spacecraft's descent is simulated using the equations of motion in Eq. 2 and, unless otherwise stated in the paper, the initial conditions reported in Table 3 are used, which include the spacecraft's parameters, such as thrust magnitude, mass, and specific impulse, and the initial orbit geometry. It is also important to note that the integration is stopped once the spacecraft reaches an altitude of 400 km, which is lower than the altitude of the LAMO, or if the spacecraft is captured into 1:1 GTR, it is stopped after 60 days.

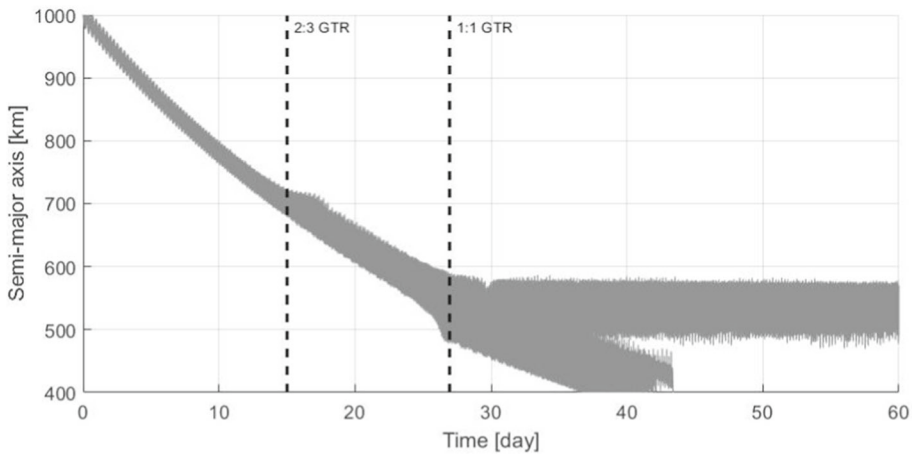


Fig. 6 Semimajor axis evolution of descent trajectories for different values of initial true anomaly. The 2:3 and 1:1 GTR locations are highlighted by the black dashed lines

The effects of the 1:1 GTR on the orbital elements of the semimajor axis, eccentricity, and inclination are investigated. Three cases are considered to understand how GTR affects the spacecraft's motion. In Tricarico and Sykes (2010) and Delsate (2012), the authors highlight the dependence and high sensitivity of the probability of capture on the initial phase of true anomaly, referred to as the initial phase throughout the paper. After a preliminary analysis, the following cases with specific values of the initial phase are considered:

- the first case considers the scenario where the spacecraft is captured within the 1:1 GTR region. The initial phase value of 72° is chosen as a reference case;
- the second case investigates the scenario where the spacecraft escapes the 1:1 GTR. The initial phase value of 0° is chosen as a reference case;
- the third case investigates the scenario where the spacecraft crosses the 1:1 GTR through the unstable equilibrium point (σ_{un} , L_{un}). The initial phase value of 70° is chosen as a reference case.

For convenience, the three cases are referred to as Test Case A (TC-A), Test Case B (TC-B), and Test Case C (TC-C), respectively.

3.1 Effects of GTRs on the semimajor axis

The effect of the GTRs on the semimajor axis is the first to be considered in this analysis. Starting from the initial semimajor axis of 1000 km, the spacecraft descends toward the target orbit at 400 km. As the spacecraft crosses the 1:1 GTR with Vesta, it can either be captured into this GTR or escape from it. Figure 6 shows the evolution of the semimajor axis for 1000 different true anomaly values.

When the spacecraft is captured into the 1:1 GTR, its semimajor axis oscillates around the GTR location. In contrast, the trajectories that escape the GTR reach toward the target semimajor axis value of 400 km. Figure 7 illustrates one such example each of a captured trajectory (top plot), an escape trajectory (middle plot), and an escape trajectory that passes through the unstable equilibrium point ($\sigma_{un} = 0$, L_{res}) (bottom plot), all of which are selected for in-depth analysis.

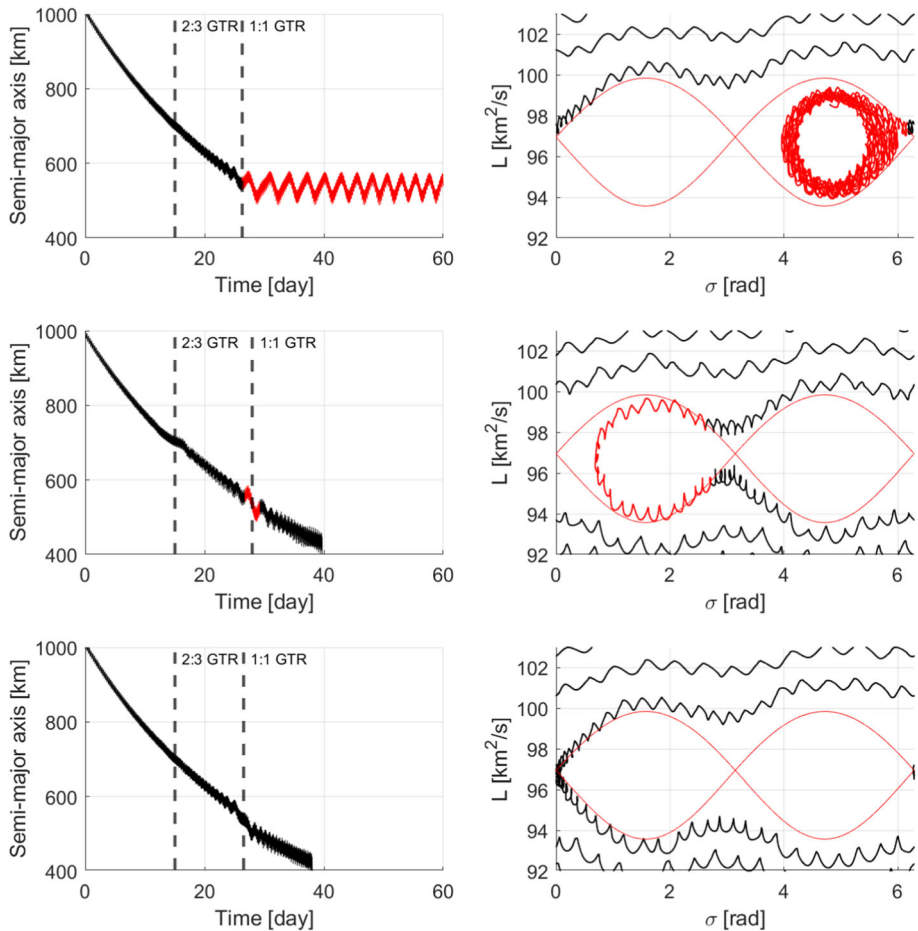


Fig. 7 The semimajor axis evolution with respect to time in TC-A, TC-B, and TC-C (on left from top to bottom) with $T = 20$ mN, and their representation in phase-space, zoomed in the 1:1 GTR region (right). In the left plots, the 2:3 and 1:1 GTR locations are highlighted by the black dashed lines. The trajectory lines are red when inside the resonance region

The main difference between the capture and escape cases lies in their different initial true anomaly values, highlighting the sensitivity of this capture phenomenon to this initial condition, as it is extensively discussed in Sect. 4. After the spacecraft is captured into 1:1 GTR, the semimajor axis (highlighted in red in the upper left plot of Fig. 7) oscillates around the location of the GTR, and the period of oscillation changes from approximately 3.6 days when the spacecraft enters the resonance (around day 30) to about 2.2 days after one month within the resonance (around day 60). The combined outcome of these effects, namely the oscillation of the semimajor axis and the decrease of the oscillation period, is reflected in phase-space as the trajectory gradually approaches closer to the equilibrium point as shown in the top right plot of Fig. 7. A trajectory that is closer to the stable equilibrium point will be farther from the separatrix, necessitating a greater thrust magnitude to successfully escape the GTR. Boumchita and Feng (2022) highlight this issue when performing an analysis of the thrust magnitude required to escape from 1:1 GTR,

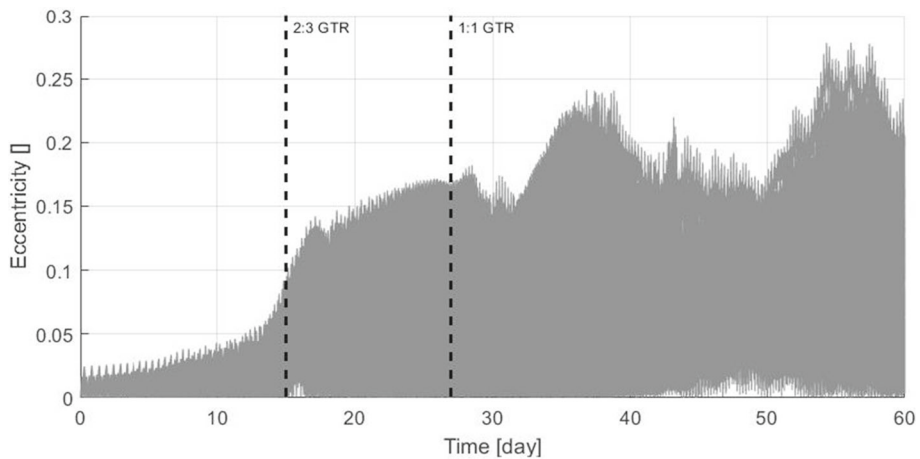


Fig. 8 Eccentricity evolution of descent trajectories for different values of initial true anomaly. The 2:3 and 1:1 GTR locations are highlighted by the black dashed lines

the time evolution of the semimajor axis is subject to significant perturbations, resulting in an increase in the libration amplitude, as shown in the lower left plot of Fig. 7. This is also shown in phase-space with the trajectory not completing a full rotation around the stable equilibrium point. Finally, the importance of considering the third case, shown in the bottom plots of Fig. 7, is highlighted in Sect. 3.3.

3.2 Effects of GTRs on the eccentricity

Delsate (Delsate 2012) identified that the 2:3 GTR is the main resonance that affected the eccentricity evolution and it is caused by the second degree tesseral harmonic. This work improves the investigation of the effect of the 1:1 GTR on the eccentricity for 1000 different initial phases uniformly sampled between 0 and 360° as shown in Fig. 8.

The eccentricity initially starts at zero and shows oscillations over time. Upon crossing the 2:3 GTR, there is a sudden increase in the eccentricity value to 0.13, which further increases to 0.15 as the spacecraft traverses the 1:1 GTR. Subsequently, the eccentricity decreases to 0.13 before increasing again to 0.2 as the spacecraft escapes the resonance. The eccentricity evolution of the three test cases are shown individually in Fig. 9.

It can be noticed that when the spacecraft crosses the 2:3 GTR, the eccentricity changes noticeably and consistently, while when the spacecraft crosses the 1:1 GTR the eccentricity continues to evolve without an identifiable extra disturbance from the resonance.

3.3 Effects of GTRs on the inclination

Figure 10 shows the inclination evolution for 1000 distinct initial phase values.

It is observed that after crossing the 1:1 GTR, the final inclination value is characterized by two types of evolutions: it either oscillates close to 90° if the spacecraft escapes the 1:1 GTR, or it decreases if the capture into the 1:1 GTR takes place. Consequently, this analysis focuses on three distinct scenarios: when the spacecraft is captured into 1:1 GTR (TC-A), when the spacecraft escapes the 1:1 GTR (TC-B) and when the spacecraft escapes the 1:1

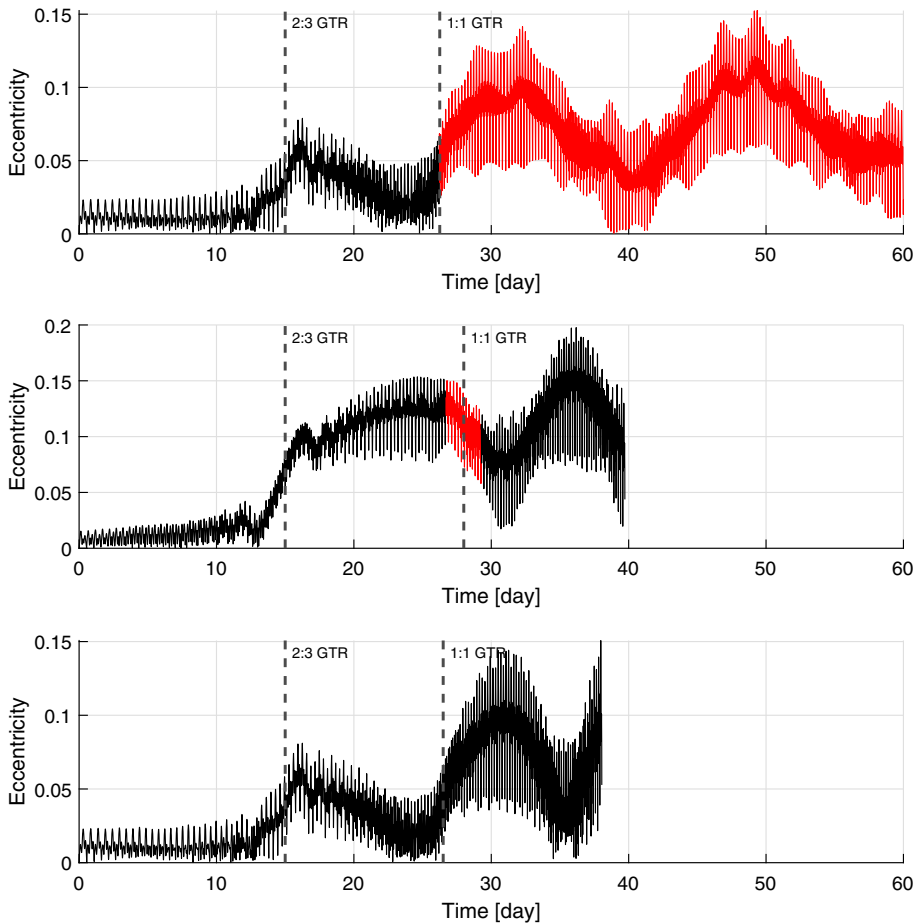


Fig. 9 Eccentricity evolution as the trajectory crosses different GTRs. The 2:3 and 1:1 GTR locations are highlighted by the black dashed lines. The top plot corresponds to TC-A, the middle one to TC-B, and the bottom one to TC-C. The trajectory lines are red when inside the resonance region

GTR through the unstable equilibrium point (TC-C). Figure 11 isolates the time evolution of the inclination for the three different test cases.

In TC-A, close to the 1:1 GTR the amplitude of the inclination oscillations increases while its mean value decreases approximately linearly with time, as shown in the top plot of Fig. 11. In TC-B, the inclination is affected by the perturbation; however, the average value remains relatively close to the initial value of approximately 90° as shown in the middle plot of Fig. 11. The 1:1 GTR has a greater influence on the inclination when the spacecraft's trajectory in phase-space passes through the unstable equilibrium point $\sigma_{un} = 0^\circ$ (bottom plot of Fig. 11). In such a scenario, the inclination undergoes a significant change, leading to an increase in its average value to approximately 92° . Figure 12 examines the impact of gravitational perturbations and low-thrust effects on the inclination evolution. The initial conditions are as outlined in Table 3, and the semimajor axis is selected to start the trajectory within the 1:1 GTR region.

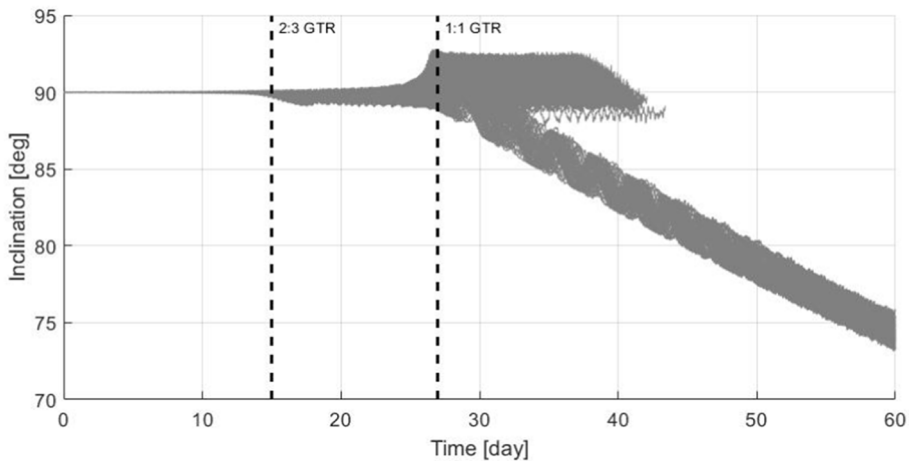


Fig. 10 Inclination evolution of descent trajectories for different values of initial true anomaly. The 2:3 and 1:1 GTR locations are highlighted by the black dashed lines

The linear trend is caused by the effect of the low-thrust acceleration and it is explained by the Gauss variational equations. In particular, the differential equation governing the inclination evolution (Curtis 2005) is

$$\frac{di}{dt} = \frac{r}{h} \cos(\omega + \theta) p_w \quad (14)$$

where h is the angular momentum and p_w is the component of the low-thrust acceleration normal to the trajectory. As the magnitude of p_w is negative the inclination decreases over time. Moreover, higher thrust magnitude results in a larger inclination change as shown in Fig. 13.

Finally, the 2:3 GTR can have varying effects on the evolution of the inclination, ranging from minimal to significant changes of a few tenths of degrees as shown in the middle plot of Fig. 11.

4 Probability of capture into GTR

This section focuses on the probability of capture into the 1:1 GTR of Dawn around Vesta, and its sensitivity on the spacecraft parameters such as the mass and thrust magnitude, and on the initial orbit geometry such as the inclination. For each semimajor axis value, 1000 trajectories are propagated for different initial phases of true anomaly values uniformly sampled in the interval $[0, 2\pi]$. With extensive simulations, this research significantly improves the understanding of the 1:1 and 2:3 GTRs by investigating their effects on varying the semimajor axis, eccentricity, and inclination, and by considering a much wider range values of thrust magnitude and spacecraft's mass. Also, this research extends the previous research by for the first time performing a systematic analysis of the sensitivity of the probability of capture into GTRs on the initial orbit geometry, the thrust magnitude, and the spacecraft's mass. The methodology and analysis performed in this work can be readily applied to a wide variety of space exploration missions.. The probabilities are obtained for the nominal orbital elements and spacecraft parameters listed in Table 3 and are shown in Fig. 14.

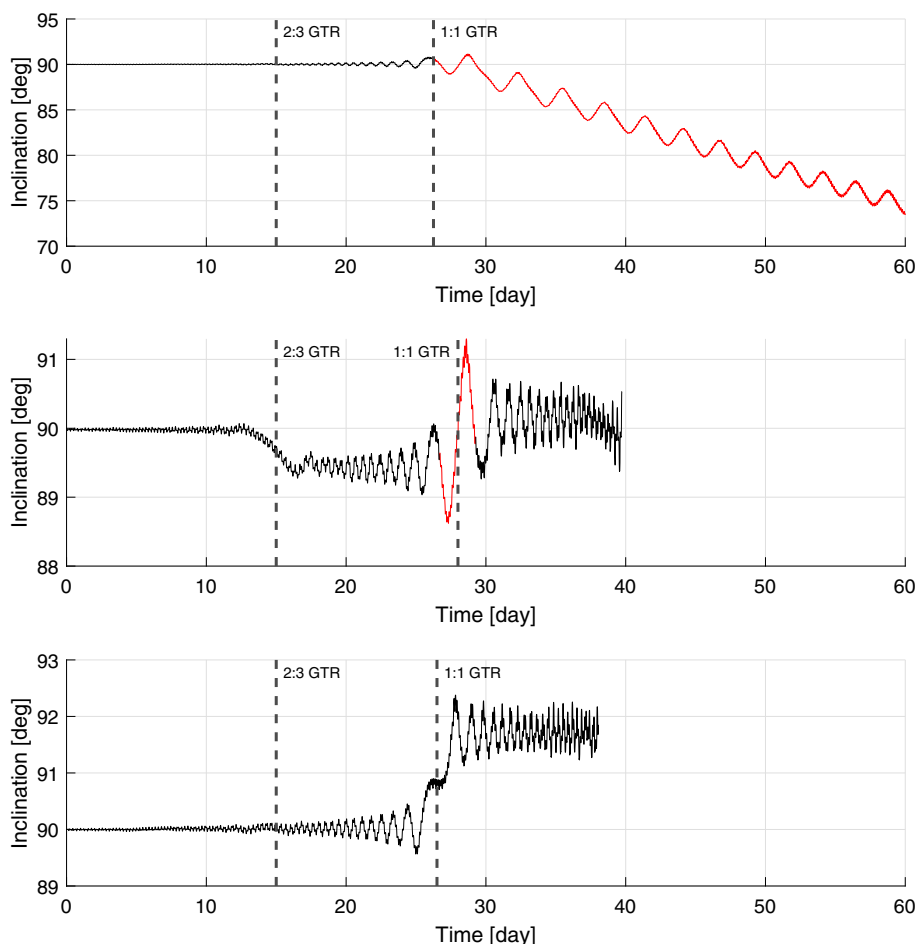


Fig. 11 Inclination evolution as the spacecraft crosses different GTRs. The upper, middle, and lower plots represent TC-A, TC-B, and TC-C, respectively. The 2:3 and 1:1 GTR locations are highlighted by the black dashed lines. The trajectory lines are red when inside the resonance region

The probability of capture into 1:1 GTR remains below 10% and no specific trend can be established as the initial semimajor axis value decreases. The average probability of capture is approximately 7.1%, with a maximum value of 9.5% and a minimum value of 4.9%. The second value is the probability of capture into the 2:3 GTR. By definition, trajectories with an initial semimajor axis of less than 700 km have a zero probability of capture into the 2:3 GTR and it is found through this set of simulations, using the specified parameters in Table 3, the spacecraft is never captured into this GTR for initial semimajor axis values larger than 700 km. When investigating the sensitivity of the probability of capture with respect to the spacecraft properties and initial orbit geometry, these results are taken as a reference.

To thoroughly explore the effects of these variables (m_0 , T , i_0 and e_0), a range of values is considered in the analysis. Dawn's dry and wet mass are, respectively, 800 and 1200 kg. The maximum value of thrust magnitude that Dawn's propulsion system could generate was 92 mN. Thus, the impact of mass and thrust magnitude on the probability of capture

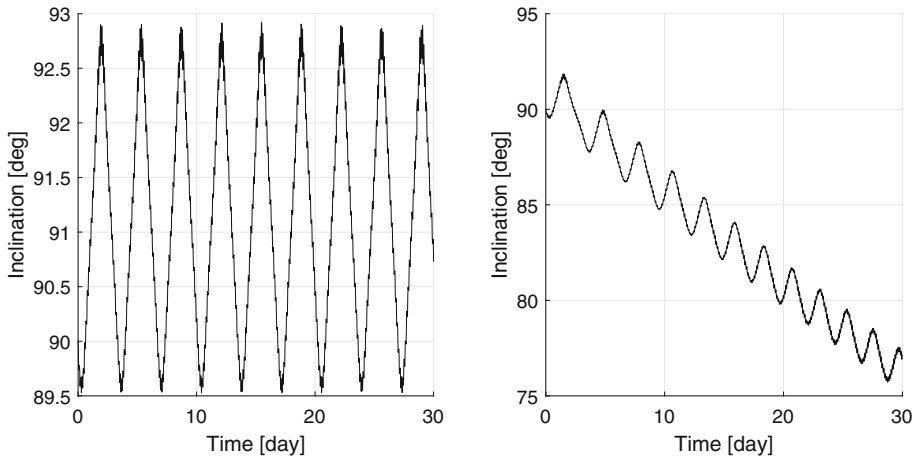


Fig. 12 Inclination evolution inside the 1:1 GTR for $T = 0$ mN (left) and $T = 20$ mN (right)

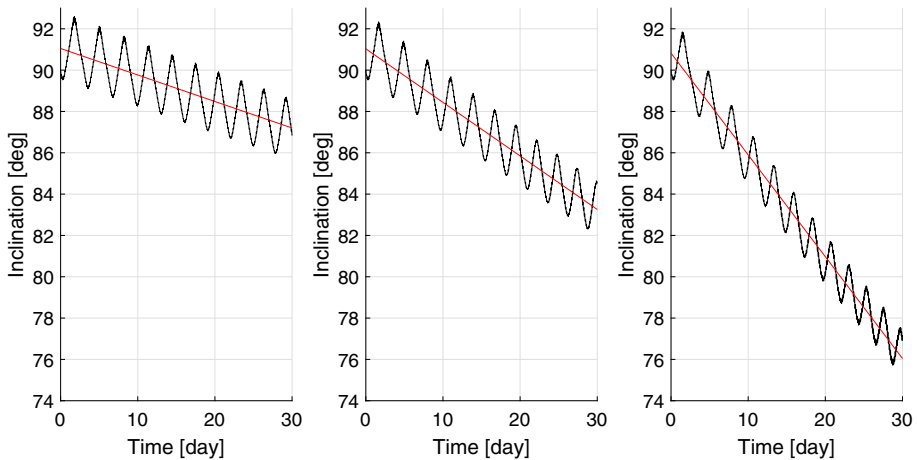


Fig. 13 Inclination evolution inside the 1:1 GTR for $T = 5$ mN (left), $T = 10$ mN (center) and $T = 20$ mN (right). The red lines represent the linear fit of the inclination evolution for each case

is studied by considering different values of mass from 800 to 1200 kg with a resolution of 50 kg and of thrust magnitude from 20 to 90 mN with a resolution of 10 mN. Concerning orbit shape and orientation, the analysis considers different initial eccentricity values, namely $[0, 0.04, 0.2]$ which are considered as null, low, and high different initial eccentricity values, and an inclination range of 0° – 180° . However, only results within the 50° – 140° range are reported in this paper, since no additional information emerges in the full range as discussed in Sect. 4.3. As for the semimajor axis, its range is selected to be between 600 (above the 1:1 GTR location) and 1000 km (corresponding to the HAMO radial distance).

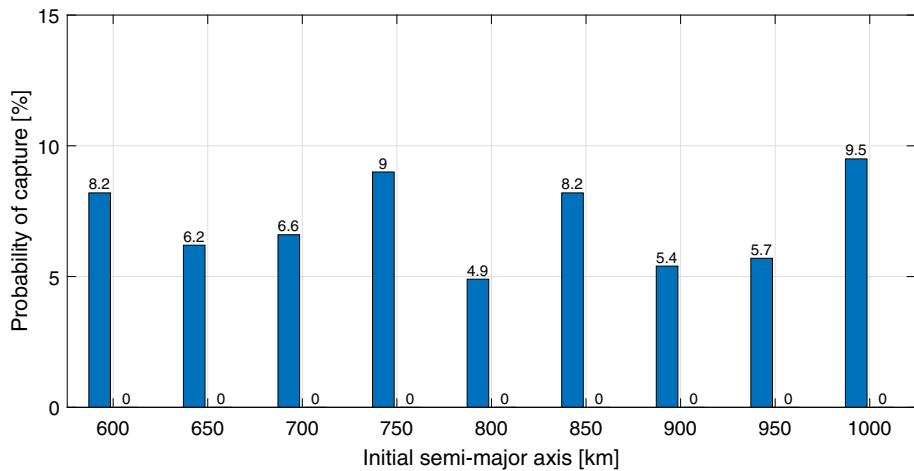
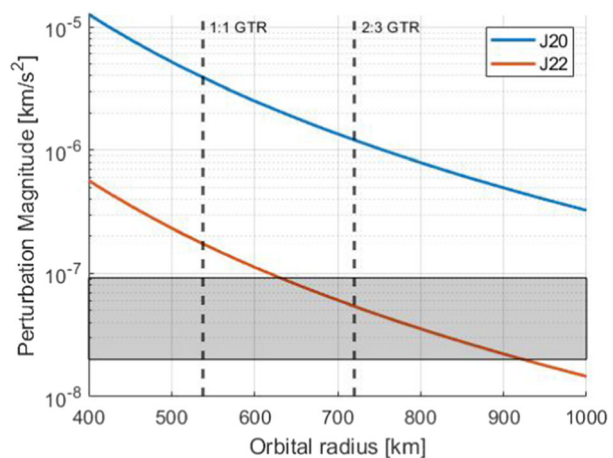


Fig. 14 Probabilities of GTR capture around Vesta in nominal conditions and at different initial semimajor axis. For each value of the semimajor axis, the first number is the probability of capture into 1:1 GTR; the second value is the probability of being captured into 2:3 GTR

Fig. 15 Magnitude of the different perturbations on Dawn at different orbital radii. The positions of the 1:1 and 2:3 GTRs have been highlighted. The gray area represents the interval of acceleration from different magnitudes of the thrust. The upper and lower limits of that area are the accelerations of 90 mN and 20 mN, respectively



4.1 Sensitivity on the thrust magnitude

By maintaining the low-thrust acceleration vector opposite to the spacecraft's velocity vector, this section analyzes the influence of thrust magnitude on the trajectory as the spacecraft descends from HAMO to LAMO. It is worth noting that the results obtained in this study depending on the thrust profile selected and the result might change with different thrust profiles. However, the methodology of this sensitivity analysis still works. In Fig. 15, the accelerations due to irregular gravitational perturbations and due to the low-thrust propulsion are compared. As the magnitude of the thrust increases, it is found that the low-thrust acceleration becomes almost comparable to the gravitational acceleration caused by the second degree tesseral harmonic, as shown in the gray region. The upper and lower bounds of the area represent the acceleration for $T = 92$ mN and $T = 20$ mN, respectively, with $m = 1000$

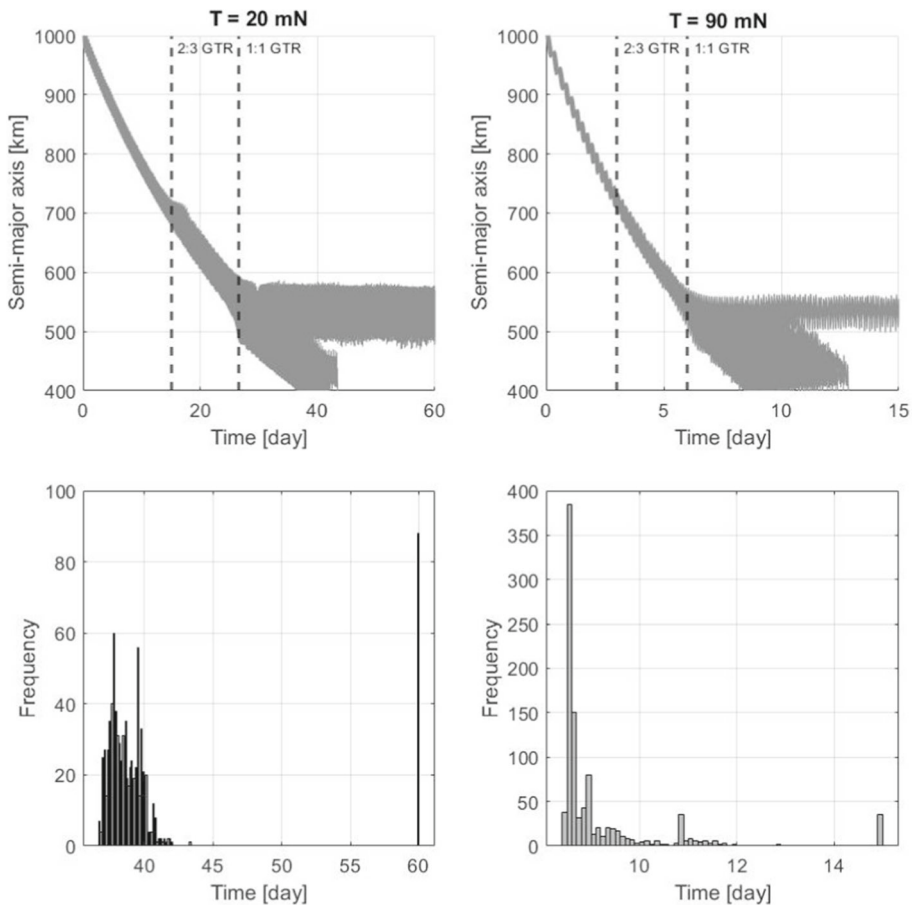


Fig. 16 Semimajor axis evolution of descent trajectories for different values of initial true anomaly for $T = 20$ mN (on the left) and $T = 90$ mN (on the right). The 2:3 and 1:1 GTR locations are highlighted by the black dashed lines. The bottom plots show the frequency of the instant in which $a = 400$ km is reached. Each bin is 0.1 days long

kg. In particular,

$$a_{LT}^{\min} = \frac{20 \times 10^{-3}}{1000} \frac{\text{N}}{\text{kg}} = 2.0 \times 10^{-8} \frac{\text{km}^2}{\text{s}} \quad (15)$$

$$a_{LT}^{\max} = \frac{92 \times 10^{-3}}{1000} \frac{\text{N}}{\text{kg}} = 9.2 \times 10^{-8} \frac{\text{km}^2}{\text{s}}. \quad (16)$$

Figure 16 shows 1000 trajectory evolutions for $T = 20$ mN and $T = 90$ mN (top plot) and two histograms of the distribution of the transfer times from HAMO to LAMO over time grouped in bins long 0.1 days (bottom plot).

For $T = 20$ mN, the distribution of the transfer times from HAMO to LAMO is concentrated between 36 and 43 days and no cases are found outside of this interval. For $T = 90$ mN, the distribution of the transfer times is concentrated between 8 and 9 days but more cases are found to reach the target orbit later. This indicates that a certain number of trajectories

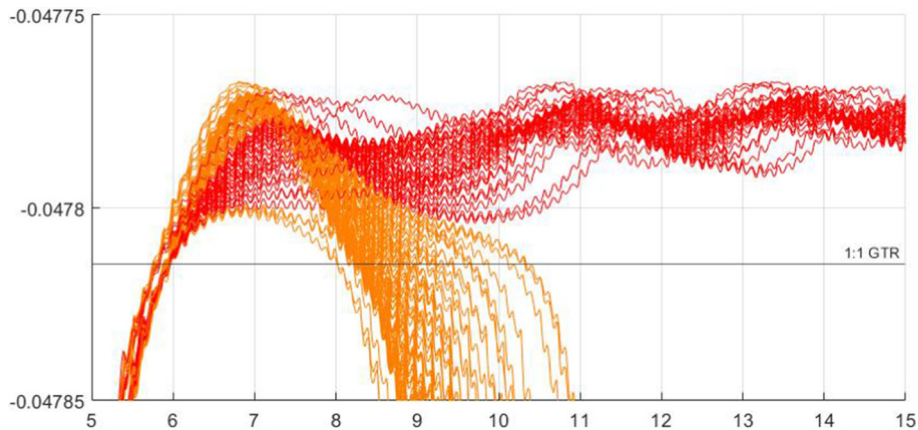


Fig. 17 Hamiltonian value of the system with respect to the 1:1 GTR energy level. The permanent and temporary capture Hamiltonian evolutions are plotted in red and orange, respectively. The horizontal black line represents the energy level of the 1:1 GTR

stay inside the resonance region for a longer time with respect to the nominal case, where the descent is completed in about 8 days before reaching the final orbit. So, for the case of $T = 20$ mN, the trajectories can be either captured or escape the resonance. Instead, for $T = 90$ mN, a third case arises in which the spacecraft reaches the final orbit while staying for a longer time inside the resonance region and being temporarily captured in it. This phenomenon is found in the field of celestial mechanics, e.g., in Henrard (1991) it was found that some pairs of satellites of Uranus have been temporarily captured into resonance in the past or in Touma and Wisdom (1998) and more recently in Vaillant and Correia (2022) it was found that the Moon was in temporary resonance with Earth and Phobos will be captured into temporary resonance with Mars, and it is now introduced in astrodynamics. In Belbruno et al. (2008), where the authors consider the temporary capture of a rock or spacecraft around the Moon in the three-body problem, the temporary capture phenomenon is defined as a capture case where the Keplerian energy of the satellite with respect to the Moon is temporarily non-positive. This definition is adapted in the context of the Dawn mission: the state of temporary capture occurs whenever the Hamiltonian value of the system with respect to the 1:1 GTR energy level (black horizontal line in Fig. 17) is temporarily positive as shown with orange lines in Fig. 17.

This phenomenon is caused by the comparability of the low-thrust acceleration and the second degree tesseral harmonic which occurs at $T = 90$ mN. For this reason, from this point, a trajectory is destined to be either permanently captured or temporary captured into resonance or escaped from the resonance. Fig. 18 isolates two cases of escape and temporary capture with $T = 90$ mN and shows their semimajor axis and inclination evolution. These cases are characterized by an initial phase angle of 0 and 60° .

The inclination in the escape case increases, leading to a final inclination value of approximately 92° (on the right plot of Fig. 18). On the other hand, in the temporary capture scenario, the inclination decreases and results in a final inclination value of approximately 83° (on the left plot of Fig. 18). This changes the value of the inclination of about 7° . A similar effect was found when the Moon was temporary captured into resonance with Earth (Touma and Wisdom 1998), during which the inclination was found to be changed by 10° with respect to Earth's equatorial plane.

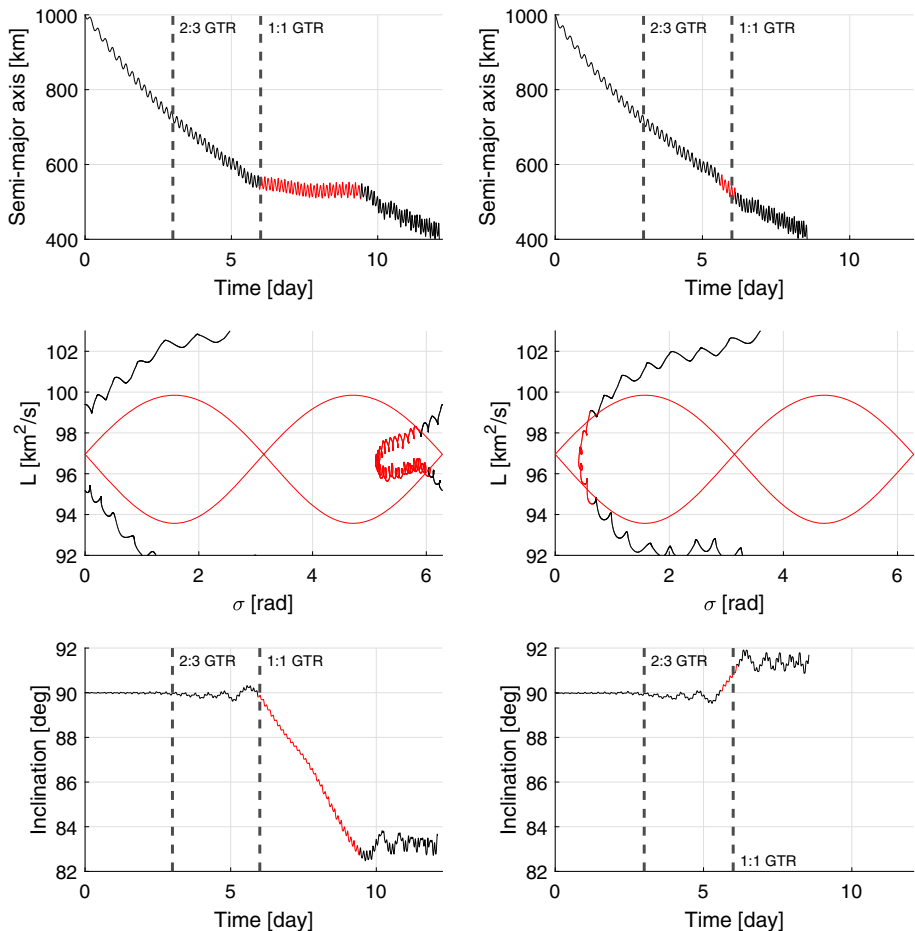


Fig. 18 Semimajor axis evolution over time (upper), in phase-space (middle) and inclination evolution over time (bottom) for descent trajectories with $T = 90$ mN. The cases of temporary capture and escape are shown on the left and right, respectively. In the upper and bottom plots, the 2:3 and 1:1 GTR locations are highlighted by the black dashed lines. The trajectory lines are red when inside the resonance region

The probability of temporary capture is estimated as a function of the initial semimajor axis value and thrust magnitude value and is shown in the matrix in Fig. 19. A histogram on the left side of the figure displays the average probability of temporary capture into the 1:1 GTR for a fixed value of thrust magnitude.

It is observed that the temporary capture phenomenon occurs when the descent is performed with higher thrust magnitudes. No temporary capture is observed at any altitude for $T = 20$ mN. As the thrust magnitude increases to 30 mN and beyond, cases of temporary capture arise if the initial semimajor axis is close to the GTR. A progressive increase in the average probability of temporary capture from approximately 1.2–4.3% has been observed as the thrust magnitude increases from 40 to 50 mN. Finally, this probability grows to 8.6% for $T = 90$ mN. The matrix of the probability of permanent GTR capture is shown in Fig. 20. As in Fig. 19, a histogram is present on the left showing the average value of the probability of permanent capture for a fixed value of thrust magnitude.

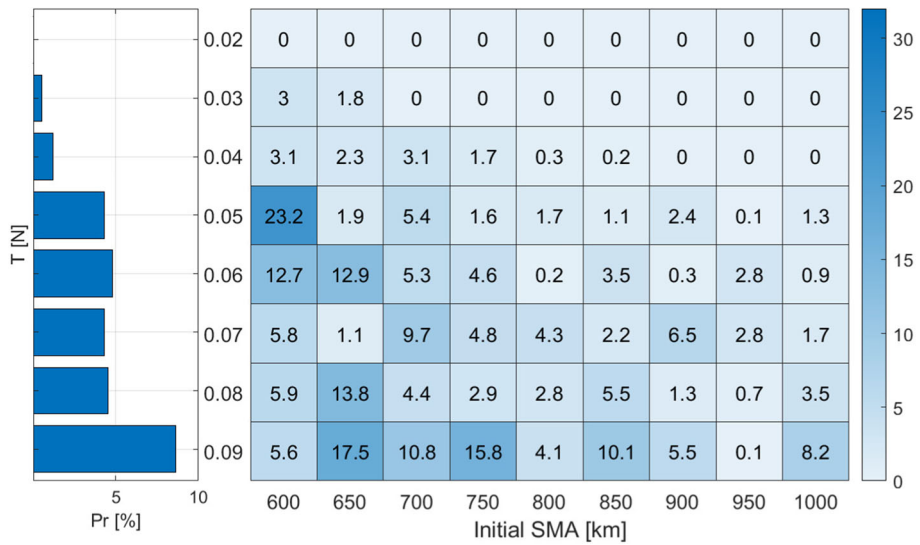


Fig. 19 Matrix of the probabilities of temporary capture into 1:1 GTR for different thrust magnitude values and initial semimajor axis. On the left, is a histogram of the mean value of the probability of temporary capture into GTR for each thrust magnitude value

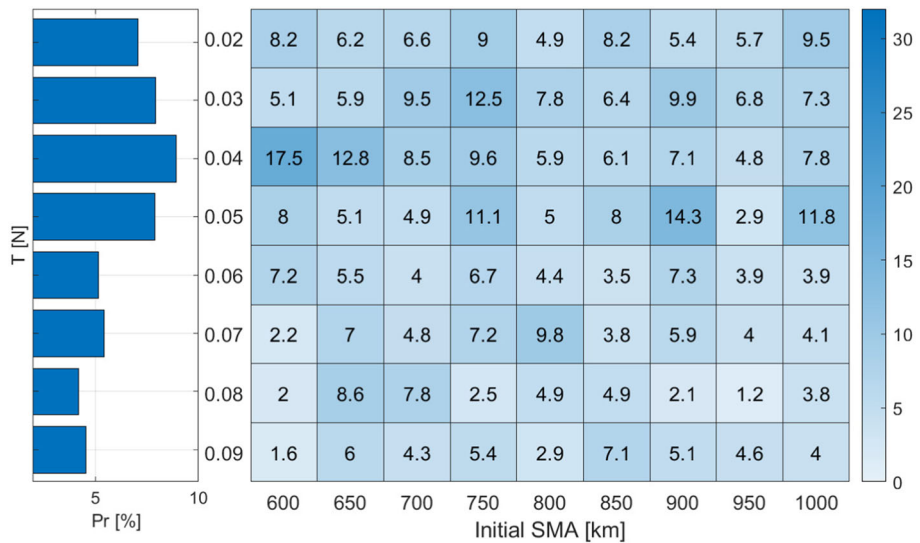


Fig. 20 Matrix of the probabilities of permanent capture into 1:1 GTR for different thrust magnitude values and initial semimajor axis. On the left, is a histogram of the mean value of the probability of permanent capture into GTR for each thrust magnitude value

This figure confirms the conclusions of Delsate (Delsate 2012) that when the motion is close to the GTR, e.g., at 600km, it is safer to descend with a thrust higher than 50 mN. By comparing the histogram plots of Fig. 19 and Fig. 20, it is concluded that, for thrust values larger than 50 mN, the probability of temporary capture increases and the probability of permanent capture decreases. Boumchita et al. (2023) shows that for very low-thrust magnitudes the probability of permanent capture is almost constant. So, the rise in temporary captures can be attributed to an increase in cases transitioning from permanent to temporary capture as the magnitude of low-thrust acceleration becomes comparable to that of the gravitational acceleration.

The correlation between the probability of permanent capture and thrust magnitude is analyzed to evaluate the relationship between the two datasets. The correlation coefficient, which indicates the linear dependence between two datasets, ranges from +1 to -1. A positive coefficient represents a positive linear dependence, meaning an increase in one variable results in an increase in the other, while a negative coefficient represents a negative linear dependence. The closer the coefficient is to +1 or -1, the stronger the linear relationship between the two datasets (Fisher 1970). The decision to focus on a linear relationship, rather than a higher-order one, is driven by the limited dataset available and the expectation that a linear regression could capture the majority of any existing correlation. Here, the Pearson correlation coefficient (Press et al. 1990) is used, which is defined as

$$\rho(\mathbf{Pr}, \mathbf{T}) = \frac{1}{N-1} \sum_{i=1}^N \left(\frac{Pr_i - \mu_{Pr}}{\eta_{Pr}} \right) \left(\frac{T_i - \mu_T}{\eta_T} \right), \quad (17)$$

where N is the dataset vector length, μ_{Pr} and η_{Pr} are the mean and standard deviation of the vector of the probability of permanent capture \mathbf{Pr} , respectively, μ_T and η_T are those of the vector of thrust magnitudes \mathbf{T} , and Pr_i and T_i are the i -th component of the vectors \mathbf{Pr} and \mathbf{T} , respectively. Depending on the value of the coefficient between the datasets, the following considerations are made (Schober et al. 2018):

- if $|\rho| < 0.2$ there is no linear correlation;
- if $0.2 < |\rho| < 0.4$ the linear correlation is weak;
- if $0.4 < |\rho| < 0.6$ the linear correlation is moderate;
- if $0.6 < |\rho| < 0.9$ the linear correlation is strong;
- if $|\rho| > 0.9$ the linear correlation is very strong.

The left plot in Fig. 21 shows the value of the correlation coefficient between the probability of permanent capture and thrust magnitude for each value of the initial semimajor axis.

All the coefficients are negative indicating the existence of a negative linear correlation between the probability of permanent capture and thrust magnitude. One case presents no correlation, one case presents a weak correlation, four cases present a moderate correlation, and three cases strong correlation. So, the majority of cases present a moderate/strong negative correlation indicating that, generally, as the thrust magnitude increases the probability of permanent capture into 1:1 GTR decreases, as shown in the right plot of Fig. 21 for the case of initial semimajor axis of 750 km.

Figure 22 shows the cases where the spacecraft is permanently captured into 1:1 GTR as a function of the initial true anomaly phase and the thrust magnitudes ranging from 20 to 90 mN, with an initial semimajor axis of 600 km. Each black point represents a specific permanent capture case corresponding to a given thrust magnitude value and initial true anomaly. Notably, these capture cases display an approximate phase shift of about 180° , particularly as thrust magnitude increases. At lower thrust levels, the capture cases are sparse and clustered

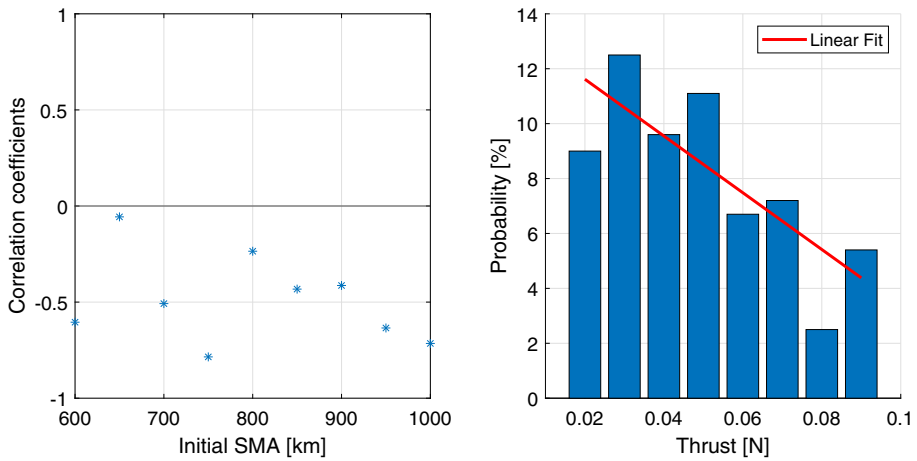


Fig. 21 The correlation coefficient between the different values of thrust and probabilities of permanent capture at different initial semimajor axis values (left). The probabilities of being permanently captured into 1:1 GTR when the descent starts at 750 km with different values of thrust (right)

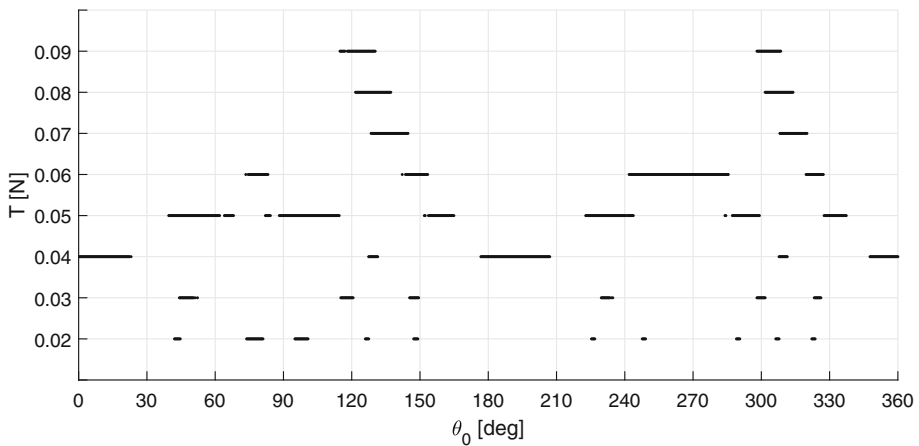


Fig. 22 Permanent capture cases (black dots) as a function of the initial true anomaly and thrust magnitude and with $a_0 = 600$ km

in narrow intervals; however, as thrust magnitude grows, these cases converge into fewer but broader groups. At higher thrust magnitudes, only two groups remain, approaching the initial true anomaly values of approximately 120° and 300° .

4.2 Sensitivity on the spacecraft's mass

During Dawn's cruise phase, approximately half of the propellant was consumed, resulting in an approximate wet mass of about 1000 kg at its arrival at Vesta (Rayman et al. 2006). In Fig. 23, the gray area represents the various low-thrust accelerations for different values of the spacecraft's mass.

Fig. 23 Order of magnitude of the different perturbations to which Dawn is subject to different orbital radii. The positions of the 1:1 and 2:3 GTRs have been highlighted. The gray area represents the interval of accelerations of the thrust considering different mass values. The upper limit is the acceleration with the $m = 800$ kg, while the lower limit corresponds to $m = 1200$ kg

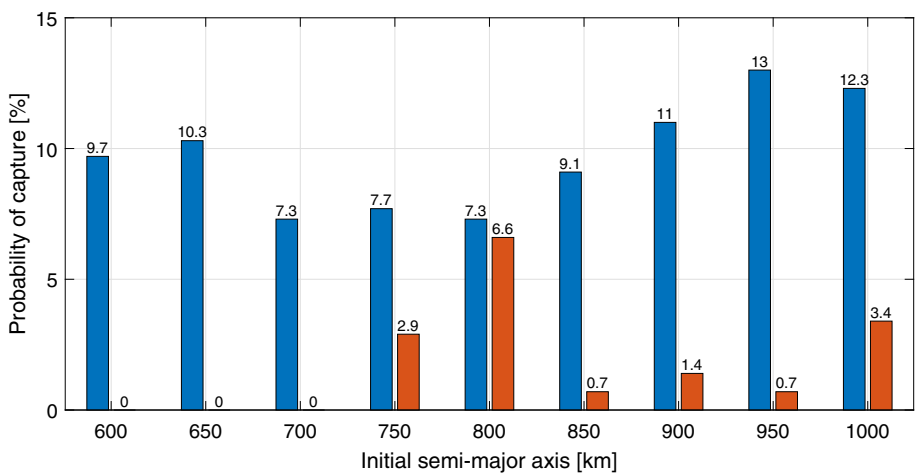
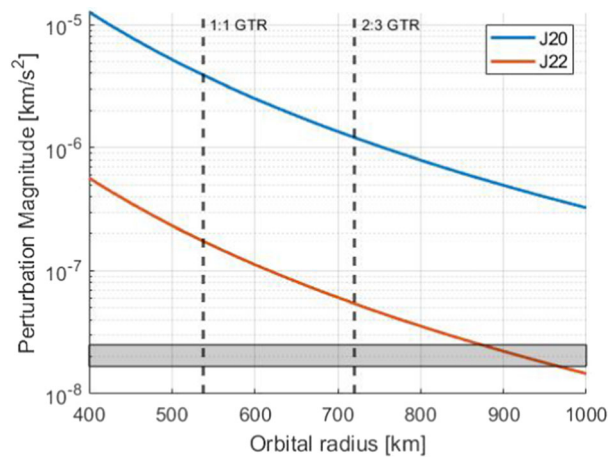


Fig. 24 Probabilities of permanent capture into GTRs around Vesta with $m = 1200$ kg at different initial semimajor axis. For each value of the semimajor axis, the first number is the probability of permanent capture into 1:1 GTR, and the second value is the probability of being permanently captured into 2:3 GTR

The lower and upper bounds of that area represent the accelerations when the mass is 1200 and 800 kg, respectively, with $T = 20$ mN. So,

$$a_{LT}^{\min} = \frac{20 \times 10^{-3} \text{ N}}{1200 \text{ kg}} = 1.6 \times 10^{-8} \frac{\text{km}^2}{\text{s}} \quad (18)$$

$$a_{LT}^{\max} = \frac{20 \times 10^{-3} \text{ N}}{800 \text{ kg}} = 2.5 \times 10^{-8} \frac{\text{km}^2}{\text{s}}. \quad (19)$$

All the low-thrust accelerations remain much lower than the acceleration due to the second degree and order harmonic, indicating that no temporary capture phenomena are expected in this part of the study. The different probabilities of permanent capture for different values of the semimajor axis are represented in Fig. 24 for $m = 1200$ kg.

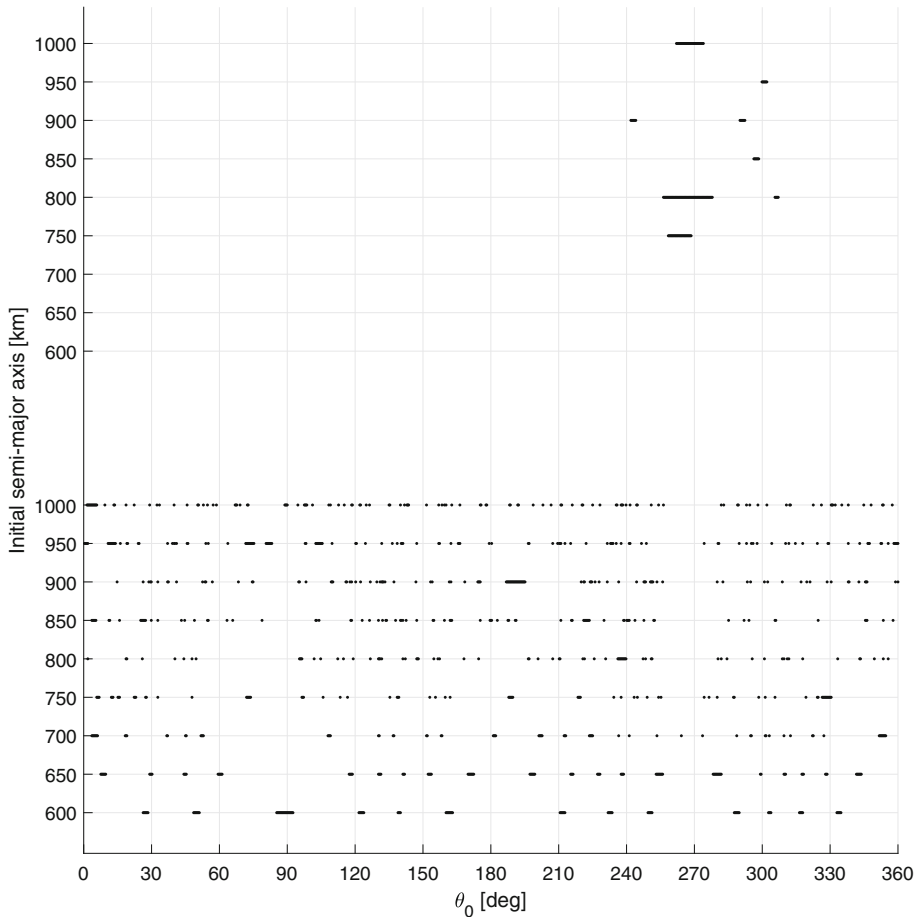


Fig. 25 Capture cases (black dots) as a function of the initial true anomaly and initial semimajor axis and with $m = 1200$ kg. The lower semimajor axis interval considers the cases of permanent capture into 1:1 GTR; while the upper interval considers the cases of capture into 2:3 GTR

The analysis reveals that the probability of permanent capture into the 2:3 GTR is highest near its location and diminishes as the initial semimajor axis increases. Concurrently, as the probability of permanent capture into 2:3 GTR rises, the probability of permanent capture into the 1:1 GTR experiences a dip around the location of the 2:3 GTR. Figure 25 shows the cases which are permanently captured into 2:3 GTR and 1:1 GTR for $m = 1200$ kg for different values of the initial phase of true anomaly in the interval between 0 and 360° . The lower interval of the semimajor axis, ranging from 600 to 1000 km, focuses on cases of permanent capture into the 1:1 GTR. Instead, the upper interval of the semimajor axis is dedicated to examining cases of permanent capture into the 2:3 GTR.

For lower initial semimajor axis values, cases of permanent capture into the 1:1 GTR are clustered into small groups, becoming increasingly sparse as the initial semimajor axis expands, as the gravitational perturbations act on the trajectory. In the context of the 2:3 GTR, the capture cases predominantly occur around the initial phase angle of 270° and within the range between 240 to 300° . As a consequence, the cases captured into 2:3 GTR will not be

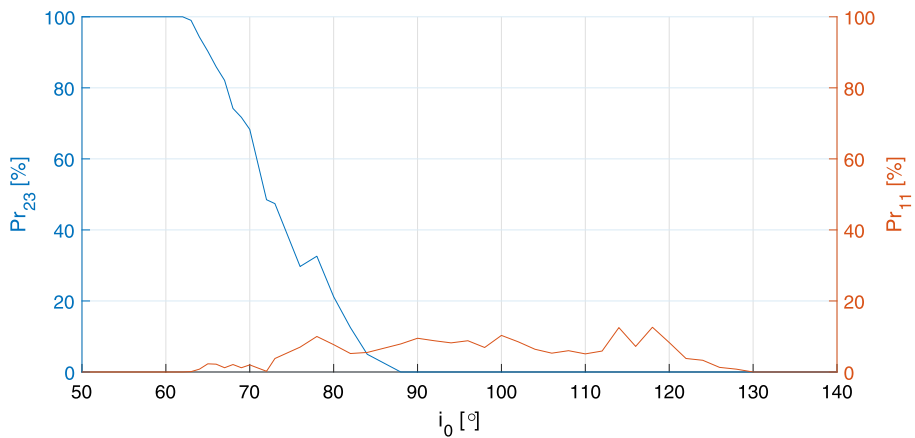


Fig. 26 Evolution of the probability of permanent capture into 2:3 (in blue) and 1:1 (in red) GTRs for different initial inclination values

captured into 1:1 GTR. It is interesting to notice that the capture into 1:1 GTR is characterized by a phase shift of 180° (see Fig. 22), while in the cases of capture into 2:3 GTR (see Fig. 25) this shift is not shown. This is a consequence of the phase-space structure of the two GTRs. In particular, the 1:1 GTR is characterized by two resonance regions between $\sigma = [0, 2\pi]$, while the 2:3 GTR is characterized by only one resonance region in the same resonance angle interval.

4.3 Sensitivity on the initial inclination

The descent of the Dawn spacecraft to LAMO started from a polar orbit. In this section, the effect of initial inclination on the probability of GTR capture is analyzed. The evolution of the probability of permanent capture into the 1:1 and 2:3 GTRs, as a function of the initial inclination in the interval of $i_0 = [50^\circ, 140^\circ]$, is shown in Fig. 26. The blue line represents the probability of permanent capture into 2:3 GTR and the red line corresponds to the probability of permanent capture into 1:1 GTR.

It is observed that if the initial inclination, $i_0 < 63^\circ$, and $e_0 = 0$, all the propagated trajectories are permanently captured into 2:3 GTR. In Sinclair (1972), this phenomenon is called “automatic entry into libration” and it occurs when the probability of capture is 100%. Neishtadt Neishtadt (1975) discussed and motivated this mechanism for Saturn’s satellite system, identifying the cause in the Hamiltonian’s singularity ($e = 0$). In fact, considering the circular and equatorial case, the Hamiltonian of the 2:3 GTR (Delsate 2012) is

$$\mathcal{H}_{2:3} = -\frac{\mu^2}{2L^2} - \frac{21}{2}eR_e^2\frac{\mu^4}{L^6}C_{22}\cos[3(M+\omega)-2\theta-\omega] + \dot{\theta}\Lambda. \quad (20)$$

The same singularity is present in this case which brings about the “automatic entry into libration” phenomenon. The second term of Eq. 20 depends explicitly on the eccentricity and as e decreases, the contribution from the tesseral harmonic decreases and disappears for $e = 0$. For $i_0 > 63^\circ$, the probability of permanent capture into 2:3 GTR decreases, while the probability of permanent capture into 1:1 GTR increases. When i_0 is close to the polar case, no trajectories are permanently captured into 2:3 GTR, while the probability of permanent capture into 1:1 GTR reaches a value of 9.5%, which was estimated in Sect. 4.

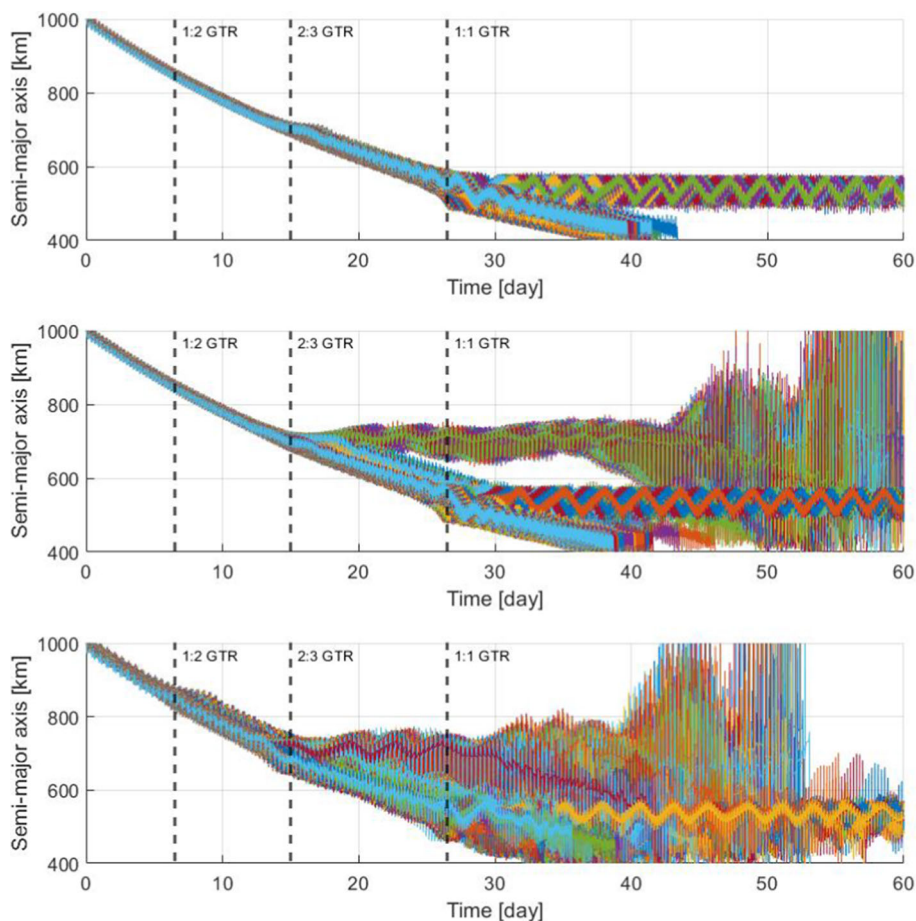


Fig. 27 Evolution of the semimajor axis in the case of $e_0 = 0$ (top), $e_0 = 0.04$ (middle) and $e_0 = 0.2$ (bottom). The 1:2, 2:3 and 1:1 GTR locations are highlighted by the black dashed lines

The probability of permanent capture into 1:1 GTR remains almost constant for higher values of i_0 and has two peak values of about 12.6% between 110° and 120° . For $i_0 > 120^\circ$, the probability of permanent capture into 1:1 GTR decreases until it reaches 0% at $i_0 = 130^\circ$, as retrograde orbits are less affected by the gravitational perturbation due to the high relative velocity between the spacecraft and the asteroid (Olsen 2006; Hu and Scheeres 2008).

4.4 Sensitivity on initial eccentricity

This section explores how the trajectory is influenced by variations in initial eccentricity. The nominal initial eccentricity for Dawn's descent toward LAMO was set to 0. Fig. 27 shows the evolution of the semimajor axis for different initial phase angles and for initial eccentricity values of 0, 0.04, and 0.2. These values are chosen to represent the scenarios of circular, low, and high eccentricity orbits, respectively. As it will be discussed later in this section, considering eccentricity values higher than 0.2 will not bring about valuable insights

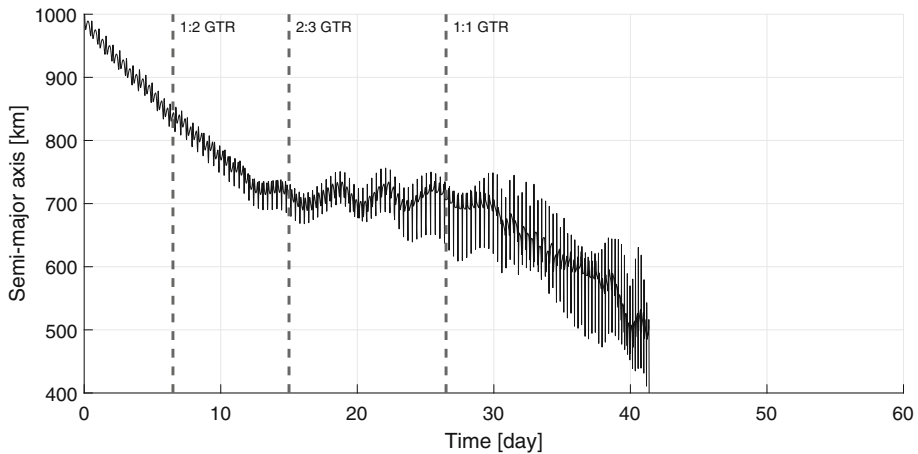


Fig. 28 Evolution of the semimajor axis in the case of an initial eccentricity of 0.2 of a trajectory temporary captured into 2:3 GTR. The 1:2, 2:3, and 1:1 GTR locations are highlighted by the black dashed lines

due to the high instability characteristics of highly eccentric orbits. To better understand the evolution of each trajectory, distinct colors (randomly assigned) are used for each trajectory, allowing the identification of specific cases of interest.

It is observed that increasing the initial eccentricity increases the risk of the spacecraft being permanently captured into the 2:3 GTR as shown in the middle plot of Fig. 27. As the initial eccentricity reaches the value of 0.2, the trajectory evolution is characterized by a large degree of instability as shown in the bottom plot of Fig. 27. For $e_0 = 0.2$, the following effects can be identified: the 1:2 GTR has a noticeable effect; the trajectories captured into 2:3 GTR are susceptible to both the cases of temporary (see Fig. 28) and permanent capture; finally, the trajectories have a probability of being temporary and permanently captured into 1:1 GTR.

Given these instability issues, discussing the probability of capture into a GTR may not be meaningful. Therefore, this section focuses on the evolution of dynamics for different initial eccentricity cases, rather than on the probability of capture into different GTRs. Since the 2:3 GTR has a strong effect on the eccentricity evolution, it is expected that the trajectories captured into this resonance are highly unstable. The instability effects are evident in the semimajor axis evolution in the cases of $e_0 = 0.04$ and $e_0 = 0.2$. In the first case, after about 25 days inside the 2:3 GTR, the semimajor axis evolution is characterized by high amplitude oscillations; in the second case, the semimajor axis oscillates after about 20 days after the trajectory is captured into 2:3 GTR. To a lesser extent, instability effects are also present in the trajectories captured into 1:1 GTR (see last 10 days of the bottom plot of Fig. 27). Finally, comparing the middle and bottom plots of Fig. 27, it is noted that the oscillations of the semimajor axis inside the 2:3 GTR increase in amplitude as the initial eccentricity increases. This phenomenon can be explained by examining the Hamiltonian corresponding to the 2:3 GTR in the polar case up to the first order in eccentricity (Delsate 2012).

$$\begin{aligned} \mathcal{H}_{2:3} = & -\frac{\mu^2}{2L^2} - \frac{15}{8}R_e^3\frac{\mu^5}{L^8}[C_{32}\sin(\sigma - \Omega) - S_{32}\cos(\sigma - \Omega)] \\ & - \frac{21}{8}eR_e^2\frac{\mu^4}{L^6}C_{22}\cos(\sigma - \omega - \Omega) + \dot{\theta}\Lambda, \end{aligned} \quad (21)$$

where $\sigma = 3(M + \omega + \Omega) - 2\theta$. Specifically, the effects of the main harmonic associated with the 2:3 GTR, $\mathcal{H}_{32} = -\frac{15}{8}R_e^3\frac{\mu^5}{L^8}[C_{32}\sin(\sigma - \Omega) - S_{32}\cos(\sigma - \Omega)]$, and the second degree and order tesseral harmonics, $\mathcal{H}_{22} = \frac{21}{8}eR_e^2\frac{\mu^4}{L^6}C_{22}\cos(\sigma - \omega - \Omega)$, should be considered. As e_0 increases, \mathcal{H}_{22} has a greater influence on the dynamics, and the resonance region corresponding to the 2:3 GTR expands. The dominant influence of \mathcal{H}_{22} with respect to \mathcal{H}_{32} is explained by analyzing the magnitude of the coefficients of each term. In the case of Vesta, the coefficients from \mathcal{H}_{22} are over three times larger with respect to the one in \mathcal{H}_{32} .

5 Conclusions

A comprehensive investigation is performed in this study to assess the effects of 1:1 and 2:3 GTRs on the semimajor axis, eccentricity, and inclination. The dynamical model includes the gravitational field of Vesta using spherical harmonics approximation up to the fourth degree and order and the low-thrust acceleration that is assumed to be opposite to the spacecraft's velocity vector direction. It is observed that the effect of both GTRs considered in this work influences the evolution of the semimajor axis; the eccentricity evolution is mostly influenced by the 2:3 GTR which results in a large variation of its value when the spacecraft crosses the 2:3 GTR; finally, the inclination is mostly influenced by the 1:1 GTR, decreasing its mean value over time as the spacecraft crossed the GTR. In addition, the effects of the spacecraft parameters (thrust magnitude and mass) and the initial orbital inclination on the probability of permanent and temporary capture into 1:1 GTR are also investigated. It is determined that the probability of permanent capture into 1:1 GTR generally decreases as the thrust magnitude. In particular for high thrust cases, the phenomenon of temporary capture is identified and its probability increases as the thrust magnitude increases. Additionally, it is observed that spacecraft with high mass values is at risk of being permanently captured into 2:3 GTR. Then, it is found that for circular orbits with initial inclinations lower than 63° all trajectories automatically enter into libration, and as the initial inclination increases, the probability of permanent capture into 2:3 GTR decreases and the probability of permanent capture into 1:1 GTR increases, reaching its maximum between 110° and 120° , after which that probability decreases to zero. Finally, the trajectory evolution is examined for null, low, and high initial eccentricity values. The analysis reveals that as initial eccentricity increases, the effects of the 2:3 GTR become more pronounced and cases of permanent capture into 2:3 GTR occur. Additionally, in cases of large initial eccentricity, the influence of other GTRs, such as the 1:2 GTR, becomes evident. For trajectories permanently captured into the 1:1 GTR, instability is observed but is generally more restricted in magnitude compared to those of trajectory permanently captured into the 2:3 GTR. It can be concluded that the case of circular and polar orbits is one of the safest options for spacecraft descent. In the future, additional investigations are recommended to design strategies for effectively leveraging GTR to achieve a desired final orbital configuration while minimizing fuel consumption. Additionally, for computational efficiency, it is recommended to develop efficient analytical or semi-analytical tools for estimating the probability of permanent capture into GTR.

Acknowledgements We would like to extend our deepest gratitude to the anonymous reviewers whose insightful comments and suggestions greatly contributed to the improvement of this manuscript. This work is funded by ESA OSIP with the project title "Resonance Capture of Low-Thrust Spacecraft Around a Small Body" and by the John Anderson Research Award Studentship of the University of Strathclyde.

Author Contributions BW and FJ wrote the main manuscript text. All authors reviewed the manuscript.

Declarations

Conflict of interest The authors declare no competing interests.

Open Access This article is licensed under a Creative Commons Attribution 4.0 International License, which permits use, sharing, adaptation, distribution and reproduction in any medium or format, as long as you give appropriate credit to the original author(s) and the source, provide a link to the Creative Commons licence, and indicate if changes were made. The images or other third party material in this article are included in the article's Creative Commons licence, unless indicated otherwise in a credit line to the material. If material is not included in the article's Creative Commons licence and your intended use is not permitted by statutory regulation or exceeds the permitted use, you will need to obtain permission directly from the copyright holder. To view a copy of this licence, visit <http://creativecommons.org/licenses/by/4.0/>.

References

- Artemyev, A.V., Neishtadt, A.I., Vainchtein, D.L., Vasiliev, A.A., Vasko, I.Y., Zelenyi, L.M.: Trapping (capture) into resonance and scattering on resonance: summary of results for space plasma systems. *Commun. Nonlinear Sci. Numer. Simul.* **65**, 111–160 (2018). <https://doi.org/10.1016/j.cnsns.2018.05.004>
- Barthelmes, F., Dietrich, R.: Use of point masses on optimized positions for the approximation of the gravity field. *Int. Assoc. Geod. Symp.* **106**, 96 (1991). https://doi.org/10.1007/978-1-4612-3104-2_57
- Belbruno, E., Toppoto, F., Gidea, M.: Resonance transitions associated to weak capture in the restricted three-body problem. *Adv. Space Res.* **42**, 1330–1351 (2008). <https://doi.org/10.1016/j.asr.2008.01.018>
- Boccaletti, D., Pucacco, G.: *Theory of Orbits, Vol. 1: Integrable Systems and Non-perturbative Methods*. Springer, Berlin (2001)
- Bouchchita, W., Feng, J., Neishtadt, A.I.: Semi-analytical estimation of the probability of capture into 1:1 ground-track resonance of a low-thrust spacecraft around an asteroid. In: 9th International Conference on Astrodynamics Tools and Techniques, Sopot (2023)
- Bouchchita, W., Feng, J.: Escape strategies from the capture into 1:1 resonance using low-thrust propulsion. In: *AAS/AIAA Astrodynamics Specialist Conference* (2022)
- Celletti, A., Gales, C.: On the dynamics of space debris: 1:1 and 2:1 resonances. *J. Nonlinear Sci.* **24**, 1231–1262 (2014). <https://doi.org/10.1007/s00332-014-9217-6>
- Celletti, A., Gales, C., Lhotka, C.: (INVITED) Resonances in the Earth's space environment. *Commun. Nonlinear Sci. Numer. Simul.* **84**, 105185 (2020). <https://doi.org/10.1016/j.cnsns.2020.105185>
- Curtis, D.H.: *Orbital Mechanics for Engineering Students*. Elsevier, Butterworth-Heinemann (2005). <https://doi.org/10.1016/C2011-0-69685-1>
- Delsate, N.: Analytical and numerical study of the ground-track resonances of Dawn orbiting Vesta. *Planet. Space Sci.* (2012). <https://doi.org/10.1016/j.pss.2011.04.013>
- Feng, J., Nooten, R., Hou, X., Visser, P., Yuan, J.: 1:1 ground-track resonance in a uniformly rotating 4th degree and order gravitational field. *Celest. Mech. Dyn. Astron.* **127**, 67–93 (2017). <https://doi.org/10.1007/s10569-016-9717-9>
- Fisher, R.A.: *Statistical Methods for Research Workers*. Haffner Press, Clawson (1970)
- Garfinkel, B.: On resonance in celestial mechanics. *Celest. Mech.* **28**, 275–290 (1982). <https://doi.org/10.1007/BF01243738>
- Goldreich, P., Peale, S.: Spin-orbit coupling in the solar system. *Astron. J.* **71**, 425–438 (1966). <https://doi.org/10.1086/109947>
- Henrard, J.: Temporary capture into resonance. In: Roy, A.E. (ed.) *Predictability, Stability, and Chaos in N-Body Dynamical Systems*, vol. 272. Springer, Berlin (1991). https://doi.org/10.1007/978-1-4684-5997-5_13
- Hu, W., Scheeres, D.J.: Numerical determination of stability regions for orbital motion in uniformly rotating second degree and order gravity fields. *Planet. Space Sci.* **52**, 685–692 (2004). <https://doi.org/10.1016/j.pss.2004.01.003>
- Hu, W., Scheeres, D.J.: Periodic orbits in rotating second degree and order gravity fields. *Chin. J. Astron. Astrophys.* (2008). <https://doi.org/10.1088/1009-9271/8/1/12>
- Huang, S., Colombo, C., Bernelli-Zazzera, F.: Low-thrust planar transfer for co-planar low earth orbit satellites considering self-induced collision avoidance. *Aerosp. Sci. Technol.* **106**, 106198 (2020). <https://doi.org/10.1016/j.ast.2020.106198>

- Kaula, W.: *Theory of Satellite Geodesy: Applications of Satellites to Geodesy*. Blaisdell Publishing Co., Waltham (1966)
- Lara, M., Russell, R.P.: Mission design through averaging of perturbed Keplerian systems: the paradigm of an Enceladus orbiter. *Celest. Mech. Dyn. Astron.* **108**, 1–22 (2010). <https://doi.org/10.1007/s10569-010-9286-2>
- Lemaître, A., Delsate, N., Valk, S.: A web of secondary resonances for large A/m geostationary debris. *Celest. Mech. Dyn. Astron.* **104**, 383–402 (2009). <https://doi.org/10.1007/s10569-009-9217-2>
- Montenbruck, O., Gill, E., Lutze, F.H.: Satellite orbits: models, methods, and applications. *Appl. Mech. Rev.* **55**(2), 27–28 (2002). <https://doi.org/10.1115/1.1451162>
- Morante, D., Sanjurjo Rivo, M., Soler, M.: A survey on low-thrust trajectory optimization approaches. *Aerospace* (2021). <https://doi.org/10.3390/aerospace8030088>
- Murray, C.D., Dermott, S.F.: *Solar System Dynamics*. Cambridge University Press, Cambridge (2000). <https://doi.org/10.1017/CBO9781139174817>
- Neishtadt, A.I.: Passage through a separatrix in a resonance problem with a slowly-varying parameter. *J. Appl. Math. Mech.* **39**, 621–632 (1975). [https://doi.org/10.1016/0021-8928\(75\)90060-X](https://doi.org/10.1016/0021-8928(75)90060-X)
- Nishiyama, K., Hosoda, S., Ueno, K., Tsukizaki, R., Kuninaka, H.: Development and testing of the Hayabusa 2 ion engine system. *Japan Soc. Aeronaut. Space Sci.* **14**, 131–140 (2016). https://doi.org/10.2322/tastj.14.Pb_131
- Olsen, O.: Orbital resonance widths in a uniformly rotating second degree and order gravity field. *Astron. Astrophys.* **449**, 821–826 (2006). <https://doi.org/10.1051/0004-6361:20054451>
- Paskowitz, M.E., Scheeres, D.J.: Design of science orbits about planetary satellites: application to Europa. *J. Guid. Control Dyn.* **29**, 96 (2006). <https://doi.org/10.2514/1.19464>
- Press, W.H., Teukolsky, S.A., Vetterling, W.T., Flannery, B.P.: *Numerical Recipes in C*. Cambridge University Press, Cambridge (1992)
- Rayman, M.D.: Lessons from the Dawn mission to Ceres and Vesta. *Acta Astronaut.* **176**, 233–237 (2020). <https://doi.org/10.1016/j.actaastro.2020.06.023>
- Rayman, M.D., Fraschetti, T.C., Raymond, C.A., Russell, C.T.: Dawn: A mission in development for exploration of main belt asteroids Vesta and Ceres. *Acta Astronaut.* **58**, 605–616 (2006). <https://doi.org/10.1016/j.actaastro.2006.01.014>
- Russell, R.P.: Global search for planar and three-dimensional periodic orbits near Europa. *J. Astron. Sci.* **54**, 199–226 (2006). <https://doi.org/10.1007/BF03256483>
- Russell, R.P., Lara, M.: On the design of an Enceladus science orbit. *Acta Astronaut.* **65**, 27–39 (2009). <https://doi.org/10.1016/j.actaastro.2009.01.021>
- Russell, C., Capaccioni, F., Coradini, A., De Sanctis, M.C., Feldmann, W., Jaumann, R., Keller, H., Mccord, T., Mcfadden, L., Mottola, S., Pieters, C., Prettyman, T., Raymond, C., Sykes, M., Smith, D., Zuber, M.: Dawn mission to Vesta and Ceres. *Earth Moon Planet.* **101**, 65–91 (2007). <https://doi.org/10.1007/s11038-007-9151-9>
- Scheeres, D.J.: Dynamics about uniformly rotating triaxial ellipsoids: applications to asteroids. *Icarus* **110**, 225–238 (1994). <https://doi.org/10.1006/icar.1994.1118>
- Scheeres, D.J.: The effect of C_{22} on orbit energy and angular momentum. *Celest. Mech. Dyn. Astron.* **73**, 339–348 (1999). <https://doi.org/10.1023/A:1008384021964>
- Scheeres, D.J.: Orbital mechanics about small bodies. *Acta Astronaut.* **72**, 1–14 (2012). <https://doi.org/10.1016/j.actaastro.2011.10.021>
- Scheeres, D.J., Ostro, S.J., Hudson, R.S., DeJong, E.M., Suzuki, S.: Dynamics of orbits close to asteroid 4179 Toutatis. *Icarus* **132**, 53–79 (1998). <https://doi.org/10.1006/icar.1997.5870>
- Scheeres, D.J., Guman, M.D., Villac, B.F.: Stability analysis of planetary satellite orbiters: application to the Europa orbiter. *J. Guid. Control Dyn.* (2001). <https://doi.org/10.2514/2.4778>
- Schober, P., Boer, C., Schwarte, L.: Correlation coefficients: appropriate use and interpretation. *Anesth. Analg.* **126**, 1763–1768 (2018). <https://doi.org/10.1213/ANE.00000000000002864>
- Shampine, L.F., Gordon, M.K.: *Computer Solution of Ordinary Differential Equations: The Initial Value Problem*. W. H. Freeman, San Francisco (1975)
- Sinclair, A.T.: On the origin of the commensurabilities amongst the satellites of Saturn. *Mon. Not. R. Astron. Soc.* (1972). <https://doi.org/10.1093/mnras/160.2.169>
- Touma, J., Wisdom, J.: Resonances in the early evolution of the Earth–Moon system. *Astron. J.* **115**, 1653–1663 (1998). <https://doi.org/10.1086/300312>
- Tricarico, P., Sykes, M.: The dynamical environment of Dawn at Vesta. *Planet. Space Sci.* **58**, 1516–1525 (2010). <https://doi.org/10.1016/j.pss.2010.07.017>
- Vaillant, T., Correia, A.C.M.: Eviction-like resonances for satellite orbits. *Astron. Astrophys.* (2022). <https://doi.org/10.1051/0004-6361/202141213>

- Valk, S., Lemaître, A., Deleflie, F.: Semi-analytical theory of mean orbital motion for geosynchronous space debris under gravitational influence. *Adv. Space Res.* **43**, 1070–1082 (2009). <https://doi.org/10.1016/j.asr.2008.12.015>
- Wallace, N., Sutherland, O., Bolter, J., Gray, H., Altay, A., Striedter, F., Budnik, F., Manganelli, S., Montagnon, E., Steiger, C.: BepiColombo—solar electric propulsion system operations for the transit to mercury. In: 36th International Electric Propulsion Conference, Vienna (2019)
- Werner, R.A.: The solid angle hidden in polyhedron gravitation formulations. *J. Geod.* **91**, 307–328 (2017). <https://doi.org/10.1007/s00190-016-0964-z>
- Whiffen, G.: Optimal low-thrust orbital transfers around a rotating non-spherical body. In: AAS/AIAA Astrodynamics Specialist Conference (2004)

Publisher's Note Springer Nature remains neutral with regard to jurisdictional claims in published maps and institutional affiliations.